Monthly Notices of the ROYAL ASTRONOMICAL SOCIETY

MNRAS **532,** 4157–4186 (2024)
Advance Access publication 2024 July 22

https://doi.org/10.1093/mnras/stae1716

Halo densities and pericenter distances of the bright Milky Way satellites as a test of dark matter physics

Kevin E. Andrade [1]★ Manoj Kaplinghat[1] and Mauro Valli[2]

[1] *University of California, Irvine, Irvine, CA 92697, USA*
[2] *INFN Sezione di Roma, Piazzale Aldo Moro 2, I-00185 Rome, Italy*

Accepted 2024 July 9. Received 2024 May 28; in original form 2023 November 2

ABSTRACT

We provide new constraints on the dark matter halo density profile of Milky Way (MW) dwarf spheroidal galaxies (dSphs) using the phase-space distribution function (DF) method. After assessing the systematics of the approach against mock data from the *Gaia* Challenge project, we apply the DF analysis to the entire kinematic sample of well-measured MW dwarf satellites for the first time. Contrary to previous findings for some of these objects, we find that the DF analysis yields results consistent with the standard Jeans analysis. In particular, in this study we rediscover (i) a large diversity in the inner halo densities of dSphs (bracketed by Draco and Fornax), and (ii) an anticorrelation between inner halo density and pericenter distance of the bright MW satellites. Regardless of the strength of the anticorrelation, we find that the distribution of these satellites in density versus pericenter space is inconsistent with the results of the high-resolution *N*-body simulations that include a disc potential. Our analysis motivates further studies on the role of internal feedback and dark matter microphysics in these dSphs.

Key words: dark matter – galaxies: dwarf – galaxies: evolution - galaxies: kinematics and dynamics.

1 INTRODUCTION

The prevailing theory of the evolution of the Universe, Lambda cold dark matter (ΛCDM), is quite successful in predicting the large scale structures we observe today. On subgalactic scales, discrepancies between predictions and observations begin to emerge (Bullock & Boylan-Kolchin 2017; Simon 2019). Among the so-called small-scale puzzles, the too-big-to-fail (TBTF) problem (Boylan-Kolchin, Bullock & Kaplinghat 2011; Kaplinghat, Valli & Yu 2019) for the observed bright dwarf spheroidal galaxies (dSphs), satellites of the Milky Way (MW) has received a lot of attention.

MW dSph galaxies are dark matter (DM)-dominated objects (Walker et al. 2006), primarily dispersion-supported (Wheeler et al. 2017), and benefit from the availability of increasingly precise stellar data thanks to instruments such as the *Gaia* satellite (Brown et al. 2018). It follows that these galaxies may represent one of the most important laboratories in order to investigate and decipher the nature of DM (for example, see recent reviews of Buckley & Peter 2018; Adhikari et al. 2022; Sales, Wetzel & Fattahi 2022).

Stars in dSphs can be typically modelled as tracers in a collisionless system. By observing their position and velocity one can draw conclusions about the nature of the underlying potential, and consequently the distribution of DM. This kind of analysis commonly employs one of three methods (Binney & Tremaine 2008; Strigari 2018; Battaglia & Nipoti 2022): (a) Jeans analysis, (b) Schwarzschild modelling, or (c) phase-space distribution function (DF) modelling.

Jeans equations relate second-order velocity moments to the density and total gravitational potential of a collisionless system (Jeans 1915; Binney & Tremaine 2008). Under the assumption of spherical symmetry, the three Jeans equations stemming from the collisionless Boltzmann equation collapse into a single one. Despite the simplification, even the spherical Jeans equation suffers from a well-known degeneracy between mass and velocity anisotropy profile of the system (Binney & Mamon 1982), and several ideas have been put forward to ameliorate this issue (see e.g. Binney & Tremaine 2008; Walker & Penarrubia 2011; Diakogiannis, Lewis & Ibata 2014; Pace et al. 2020). Utilizing moments of velocity higher than second order is one method of addressing this issue (see e.g. Łokas & Mamon 2003; Richardson & Fairbairn 2014; Kaplinghat et al. 2019; Read, Walker & Steger 2019b).

The spherical Jeans equation has been a playground for a multitude of studies on dSph kinematics (Strigari et al. 2007; Battaglia et al. 2008; Evans, An & Walker 2009; Strigari et al. 2008; Walker et al. 2009; Hayashi & Chiba 2012; Zhu et al. 2016; Diakogiannis et al. 2017; Hayashi, Chiba & Ishiyama 2020). More recently, Read et al. (2019b) used the Jeans equation solver `gravsphere` and fourth-order velocity moments to examine the inner densities of MW classical dwarfs. Kaplinghat et al. (2019) also performed a spherical Jeans analysis coupled with fourth-order velocity moments to predict the inner densities of bright MW dSphs. Chang & Necib (2021) and Guerra, Geha & Strigari (2021) used the Jeans approach to examine the inner halo density profile in simulated dwarf galaxies to eventually report that only with the radial velocity data from $\mathcal{O}(10^4)$ stars could cusps and cores could be easily distinguished.

Going back to the seminal paper of Schwarzchild (1980), orbit-based models consist of integrating particle paths in a given potential in order to create an 'orbit library'. Consequently, a numerical approximation to system's phase space DF can be obtained as a

★ E-mail: kevinea@outlook.com

© 2024 The Author(s).
Published by Oxford University Press on behalf of Royal Astronomical Society. This is an Open Access article distributed under the terms of the Creative Commons Attribution License (https://creativecommons.org/licenses/by/4.0/), which permits unrestricted reuse, distribution, and reproduction in any medium, provided the original work is properly cited.

Downloaded from https://academic.oup.com/mnras/article/532/4/4157/7718108 by UC - Irvine user on 24 July 2025

superposition of the orbit library elements (Jardel & Gebhardt 2012; Breddels et al. 2013; Breddels & Helmi 2013; Jardel et al. 2013; Kowalczyk, Łokas & Valluri 2017, 2018; Hagen, Helmi & Breddels 2019; Kowalczyk et al. 2019). Contrary to the Jeans approach, the Schwarzschild one does not require any assumption on the orbital anisotropy profile of the system that can be a posteriori computed without any a priori ansatz. For this reason, the Schwarzschild modelling has been adopted to some extent to analyse mock and observed MW dSph kinematic data (Van Den Bosch et al. 2008; Breddels et al. 2012; Jardel & Gebhardt 2012; Jardel et al. 2013; Kowalczyk et al. 2017; Kowalczyk & Lokas 2022, as examples). The Schwarzschild method is quite general, relying essentially on the assumption of dynamical equilibrium for the system and on the geometry of the problem. Nevertheless, it remains computationally demanding once a marginalization over unknowns related to the assumed total gravitational potential has to be performed. Additionally, it has the additional drawback of yielding an approximated DF intelligible only numerically.

Differently from methods (a) and (b), method (c) – the phase-space DF approach – requires an analytic ansatz in six dimensions (3 in position, 3 in velocity) for the probability distribution of the stellar system in their DM potential. The ansatz is typically obtained exploiting Jeans' theorem, i.e. expressing the DF via the integrals of motion. This approach allows for flexible forms for the stellar distribution, and can also allow consideration of velocity moments above second order, potentially mitigating the mass-anisotropy degeneracy of the spherical Jeans analysis. As examples, Wu & Tremaine (2006) used the DF method to derive the mass distribution of Messier 87 using its globular clusters as tracers. More recently, regarding the case of MW dSphs Strigari, Frenk & White (2017) used an approximate DF model to examine the DM profile of the Sculptor dwarf galaxy.

Recent examples of hybrid applications of the DF approach with the Jeans equation can be found in Lokas, Mamon & Prada (2005), Łokas (2009), Strigari, Frenk & White (2010), Battaglia, Helmi & Breddels (2013), Breddels & Helmi (2013), Ferrer & Hunter (2013), Lacroix, Stref & Lavalle (2018), Petac, Ullio & Valli (2018), Li et al. (2020), Li & Widrow (2021), and Read et al. (2021). On top of that, examples of studies utilizing multiple chemo-dynamical populations are also present in the literature (see Battaglia et al. 2008; Agnello & Evans 2012; Amorisco & Evans 2012; Zhu et al. 2016; Strigari et al. 2017; Pascale et al. 2018).[1]

The central profiles and densities of dwarf galaxies have long presented challenges to the ΛCDM model of galaxy formation (Salucci & Burkert 2000; Hayashi et al. 2003; Governato et al. 2010; Weinberg et al. 2015). More recently, it has been asserted that there is an anticorrelation between the central densities of the MW dSphs and their pericentre distances (Kaplinghat et al. 2019). In this work, we reexamine that relationship. Here, we apply the DF method to the kinematic data of the bright MW dSphs with the aim of providing a new, theoretically broad study of the DM content in these galaxies that is completely decoupled and, hence, complementary to the Jeans approach, along the lines of what was carried out originally in Strigari et al. (2017). In order to validate our modelling method, we first examine 32 mock data sets of various configurations from the Gaia Challenge project (Read, Gieles & Kawata 2019a). We then analyse the bright dSphs of the MW: Draco, Fornax, Sculptor, Carina, Sextans, Leo I, Leo II, Ursa Minor, and Canes Venatici I. We show that with the DF approach it is possible to constrain the DM halo of these galaxies in the inner regions with similar precision to the one previously obtained in literature with the Jeans approach (Kaplinghat et al. 2019; Read et al. 2019b). We have chosen to use the DM density at 150 pc, ρ_{150}, as the key metric for inner density. While not perfect, it is a good parameter for encapsulating the inner density for haloes in this size range, and is at a radial position that lends itself well for inferences by stellar data. Moreover, it was used by several prior authors (Read et al. 2018, 2019b; Kaplinghat et al. 2019; Hayashi et al. 2020) and thus facilitates comparisons.

A key result of this work is an inference of the inner density of the bright MW dSphs using a uniform set of priors and a generalized DF. It serves as a test of dark matter physics [see recent work, for instance, Valli & Yu (2018); Read et al. (2018); Kaplinghat et al. (2019); Nadler et al. (2019, 2021a, b); Correa (2021); Kim & Peter (2021); Slone et al. (2021); Yang, Nadler & Yu (2023)] and provides constraints on dark matter models [see the recent review of Adhikari et al. (2022) in this regard]. In particular, we show that the central densities (inferred within 150 pc) of the bright MW dSphs vary by a factor of ∼5, with Fornax and Carina on the low end, and Draco and Leo I on the high end.

When the inner densities of the MW dSphs are compared to their pericenter distances, an interesting anticorrelation emerges (Kaplinghat et al. 2019). We re-examine and confirm this relation. The distribution of the MW dSphs in the density-pericenter plane appears to be in stark conflict with the result of the 'Phat Elvis' *N*-body simulation in Kelley et al. (2019), which examined MW-like haloes with a disc potential. This is our second key result: we find that the distribution of the bright MW dSphs in density-pericenter space is starkly inconsistent with high-res ΛCDM *N*-body simulation results. Solutions to the TBTF problem and, in general, all particle physics models that predict deviations on subgalactic scales from the ΛCDM model should include information about the orbits of dSphs when looking for consistency with dark matter density inferences.

This paper is organized as follows: Section 2 develops the theory of the DF approach and lays the foundation for our statistical analysis. In Section 3, we present the mock data validation. Section 4 contains the results of applying the model to the bright MW dSphs, and, in particular, constraints on $r_{\rm max}$ and $V_{\rm max}$. In Section 5, we zoom on Draco and Fornax as representatives of the diversity among the bright MW dSphs emerging from our DF approach. In Section 6, we detail our inference for all the bright dSphs of $r_{\rm max}$, $V_{\rm max}$, ρ_{150}, as well as mass estimates within various radii, offering also a direct comparison with the recent studies on the subject based on the Jeans approach. We examine the anticorrelation of ρ_{150} and pericenter distance in Section 7. We present our conclusions in Section 8. Further details on our analysis and interesting cross-checks related to our study can be found in Appendices A–O.

2 DF MODELS

Let us start by describing our approach in modelling the stellar and DM distributions in dSphs. It is possible to describe the position and velocity of stars (or other objects) in a galaxy using a phase-space DF in six dimensions, three for position and three for velocity. Our intent is to use DFs to analyse the bright dSphs of the MW, using the stars as tracers to determine the DM distribution.

We define a Cartesian coordinate system, centred on the galaxy centre, with the z-axis along the line of sight (LOS) to the system. The projected radius of a star as seen from the observer is then $R = \sqrt{x^2 + y^2}$. An individual star will have a position coordinate $\boldsymbol{x}$, given by (x, y, z). The star will have a velocity vector $\boldsymbol{v}$, with

[1]Regarding this point, in this work we will not entail any metallicity distinction in the stellar population of an MW satellite.

Downloaded from https://academic.oup.com/mnras/article/532/4/4157/7718108 by UC - Irvine user on 24 July 2025

components (v_x, v_y, v_z). We also define η to be the angle between $\boldsymbol{x}$ and $\boldsymbol{v}$.

We can introduce the DF f such that $f(\boldsymbol{x}, \boldsymbol{v}, t)\mathrm{d}^3\boldsymbol{x}\ \mathrm{d}^3\boldsymbol{v}$ is the probability of finding a star in the infinitesimal volume element $\mathrm{d}^3\boldsymbol{x}\ \mathrm{d}^3\boldsymbol{v}$. Under the assumption of dynamical equilibrium, the DF can be regarded as constant in time, $f(\boldsymbol{x}, \boldsymbol{v})$. We require DF to be normalized to one over all phase space according to the definition of probability distribution.

Motions of particles like stars in a stationary potential can be determined by the collisionless Boltzman equation. Under the approximation of spherical symmetry, the Strong Jeans Theorem then tells us that solutions to the collisionless Boltzman equation depend only upon two integrals of motion, the orbital energy E, and the total angular momentum L (Binney & Tremaine 2008).

Given a spherically symmetric potential Φ, the energy of a star per unit mass is given by $E(r, v) = \Phi(r) + v^2/2$, and the angular momentum per unit mass corresponds to $L(r, v) = rv\ \sin\eta$. Several useful quantities can be derived from the DF, including the density profile, the radial velocity dispersion profile, and the tangential velocity dispersion profile (Binney & Tremaine 2008; Strigari et al. 2017):

$$\mu(r) = \int \mathrm{d}^3\boldsymbol{v}\ f(x, v) = 2\pi \int_0^{\pi} \mathrm{d}\eta\ \sin\eta \int_0^{v_{\rm lim}} \mathrm{d}v\ v^2\ f(E, L), \quad (1)$$

$$\sigma_{\rm r}^2(r) = \frac{2\pi}{\mu} \int_0^{\pi} \mathrm{d}\eta\ \sin\eta\ \cos^2\eta \int_0^{v_{\rm lim}} \mathrm{d}v\ f(E, L)\ v^4, \quad (2)$$

$$\sigma_{\rm t}^2(r) = \frac{\pi}{\mu} \int_0^{\pi} \mathrm{d}\eta\ \sin^3\eta\ \int_0^{v_{\rm lim}} \mathrm{d}v\ f(E, L)\ v^4, \quad (3)$$

We define $\mu(r)$ as the probability per unit volume of finding a star at radius r. The number density of stars at radius r is then

$$n(r) = w\ \mu(r), \quad (4)$$

where w is the total number of stars in the population. We define the velocity above which stars become unbound as $v_{\rm lim} = \sqrt{2(\Phi_{\rm lim} - \Phi(r))}$, where $\Phi(r)$ and $\Phi_{\rm lim}$ are given explicitly in Section 2.1 for specific cases that are relevant for our analysis. The total velocity dispersion can be found by combining the radial and tangential components:

$$\sigma_{\rm tot}^2(r) = \sigma_{\rm r}^2(r) + 2\sigma_{\rm t}^2(r). \quad (5)$$

The projected stellar density Σ_* at a radius R can be found by integrating over the LOS:

$$\Sigma_*(R) = 2\int_0^{\infty} \mathrm{d}z\ n(r), \quad (6)$$

where $r = z^2 + R^2$. The LOS velocity dispersion can be found from

$$\Sigma_*(R)\ \sigma_{\rm LOS}^2(R) = 2\int_0^{\infty} \mathrm{d}z\ n(r) \frac{z^2\sigma_{\rm r}^2 + R^2\sigma_{\rm t}^2}{z^2 + R^2}$$
$$= 2\pi w \int_0^{\pi} \mathrm{d}\eta\ \sin\eta \int_0^{v_{\rm lim}} \mathrm{d}v v^4$$
$$\cdot \int_0^{\infty} \mathrm{d}z \frac{(2z^2\cos^2\eta + R^2\sin^2\eta)}{z^2 + R^2} f(E, L), \quad (7)$$

Higher order moments of velocity can also be predicted by this method. We will use a VSP that is the fourth moment of velocity in our analysis. For our purposes we opt to compute the global VSP rather than one that varies with radius, which helps to minimize noise in the calculation. The derivation of the VSP is presented in Appendix B.

2.1 Halo DM profiles

We consider here the total stellar mass of the system to be negligible in comparison to that of the DM – a good approximation for the study of MW dSphs – and so the stars are tracers of the DM potential but do not influence it. We will consider three potential/density profiles: 'NFW', 'cored', and 'cNFW'. The NFW and cored profiles can be completely described by two parameters, while the cNFW profile has one additional parameter, the core parameter 'c'. The cNFW core parameter $c \equiv r_{\rm c}/r_{\rm s}$, where $\log_{10}[r_{\rm c}/{\rm kpc}]$ is the parameter used in the model (which we distinguish from the core radius $r_{\rm core}$, defined below). We also use the scale radius $r_{\rm s}$ and scale velocity $v_{\rm s}$ as specifying parameters for all three profiles. The scale density $\rho_{\rm s}$ and the scale potential $\Phi_{\rm s}$ are determined via the relation $\Phi_{\rm s} = v_{\rm s}^2 = 4\pi G r_{\rm s}^2 \rho_{\rm s}$, where G represents Newton's gravitational constant.

Let $x \equiv r/r_{\rm s}$. The NFW profile density and potential pair is then

$$\rho(r) = \frac{\rho_s}{x(x+1)^2}\ , \quad (8)$$

and the corresponding gravitational potential becomes

$$\Phi(r) = \Phi_{\rm s}\left(1 - \frac{\log(x+1)}{x}\right)\ . \quad (9)$$

Note that Φ has been defined so that it is non-negative everywhere, with a value of zero at $r = 0$, and goes to $\Phi_{\rm s}$ as $r \to \infty$.

Define the peak circular velocity in a potential as $V_{\rm max}$, and the radius at which the peak occurs as $r_{\rm max}$. For the NFW profile, it can be shown that $r_{\rm max} = 2.163\ r_{\rm s}$, and $V_{\rm max} = 0.465\ v_{\rm s}$.

The 'cored' profile is a generalized Hernquist profile (Hernquist 1990; Zhao 1996) of the form

$$\rho(r) = \frac{\rho_s}{(x+1)^3}\ , \quad (10)$$

with underlying gravitational potential

$$\Phi(r) = \Phi_{\rm s} \frac{x\,(x+2) - 2\,(x+1)\log\,(x+1)}{2x\,(x+1)}\ .$$

The potential in the cored case has a zero value at $r = 0$, and goes to $\Phi_{\rm s}/2$ as $r \to \infty$. For the cored case, $r_{\rm max} = 4.4247\ r_{\rm s}$, and $V_{\rm max} = 0.3502\ v_{\rm s}$.

The cNFW profile is defined as

$$\rho = \frac{\rho_{\rm s}}{(x+c)\,(x+1)^2}\ , \quad (11)$$

with potential being

$$\Phi(r) = \frac{\Phi_{\rm s}}{(c-1)^2}\left(\frac{x\,(c-1)}{(x+1)} + (1-2c)\log(x+1) + c^2\log\left(\frac{c+x}{c}\right)\right).$$

This profile reduces to the canonical NFW form for $c \to 0$ and reduces to the cored form when $c \to 1$. The relation for conversion between $r_{\rm s}$ and $r_{\rm max}$ (and similarly between $v_{\rm s}$ and $V_{\rm max}$) becomes non-linear but can be solved numerically.

For all profiles, we define the core radius $r_{\rm core}$ as the radius at which the DM density falls to 50 per cent of its central value. For the NFW profile there is no core radius. For the cored profile, $r_{\rm core}$ is $0.26\ r_{\rm s}$. For the cNFW profile, the core radius is a nonlinear function of c to be computed numerically. Finally, we define Φ_∞ as the value of the potential as $r \to \infty$.

2.2 Stellar DF form

We take the form of the stellar DF to be the product of an energy function and an angular momentum function, following the ansatz

Downloaded from https://academic.oup.com/mnras/article/532/4/4157/7718108 by UC - Irvine user on 24 July 2025

Table 1. Parameter limits for the top-hat priors in our MCMC analysis. Units are kpc for r_s and r_c, and km s^{-1} for v_s. The units for w are the number of stars in the population. The other parameters are dimensionless. The parameters $\tilde{E}_c$ and $\tilde{\Phi}_{lim}$ are made dimensionless by dividing by Φ_∞ for the distribution being used, and $\tilde{L_\beta}$ is made dimensionless by dividing by $r_s\sqrt{\Phi_\infty}$.

	$\log_{10}(\frac{r_s}{kpc})$	$\log_{10}(\frac{v_s}{km/s})$	$\log_{10}(\frac{r_c}{kpc})$	a	q	$\tilde{E}_c$	d	$\tilde{\Phi}_{lim}$	e	$\tilde{L_\beta}$	b_{in}	b_{out}	α	$\log_{10}(\frac{w}{stars})$
Lower limit	−2.5	0	−2	−4	0.1	0.01	−12	0.01	0.1	0.01	−10	−10	0.1	1
Upper limit	1	2.5	1	5	25	1	0	1	10	1	10	10	10	7

$$h(E) = \begin{cases} E^a(E_c^q + E^q)^{d/q}(\Phi_{lim} - E)^e, & E < \Phi_{lim} \\ 0, & E \geq \Phi_{lim} \end{cases} \quad (12)$$

$$g(L) = \left(\frac{1}{2}\left(\left(\frac{L}{L_\beta}\right)^{\frac{b_{in}}{\alpha}} + \left(\frac{L}{L_\beta}\right)^{\frac{b_{out}}{\alpha}}\right)\right)^{\alpha}, \quad (13)$$

with α non-negative for $b_{in} <= b_{out}$ and α negative for $b_{in} > b_{out}$. The total DF is their normalized product:

$$f(E, L) = n_f\, h(E)\, g(L), \quad (14)$$

that multiplied by w yields the total phase-space density distribution of w stars. In these equations, n_f is a normalizing factor that ensures that the DF integrates to unity over all phase space, i.e.

$$n_f = \left(\int h(E)g(L)\,d^3x\,d^3v\right)^{-1}. \quad (15)$$

The normalization factor is required so that the DF can be interpreted as a probability density for finding a particle in a given location in phase space. It is computationally expensive, because it is a multidimensional integral that must be calculated at every iteration in a Monte Carlo Markov Chain (MCMC) analysis. It might be argued that n_f changes little as the chain converges, so that its calculation at every iteration is unnecessary. However, we found that changes did indeed impact on the results, possibly through an impact on the shape of the prior volume, and it is therefore necessary to calculate at every iteration of the parameters.

Note that these expressions correspond closely to those reported in Strigari et al. (2017), except we have inserted a factor of 1/2 in the angular momentum function to ensure that the function transitions smoothly as α changes sign, avoiding any parametric discontinuity in our ansatz. We compare the results of Strigari et al. (2017) with ours in Appendix A. The parameter Φ_{lim} is a limiting potential beyond which no stars exist, analogous to a tidal cut-off potential, and we define r_{lim} as the radius at which this cut-off occurs for a particle with zero velocity. The e parameter controls the shape of the tidal cut-off. The parameters a and d control the log-slope of the energy response. E_c is a cut-off energy, below which the log-slope is approximately a, and above which the log-slope is approximately $a + d$. We restrict d such that $d < 0$.

The parameter L_β characterizes the angular momentum scale, and the parameters b_{in} and b_{out} control the inner and outer log-slopes of the angular momentum function, respectively. At angular momenta $\gg L_\beta$, the log-slope is approximately b_{out}, and for angular momenta $\ll L_\beta$ the slope is approximately b_{in}. As a result, the parameters b_{in} and b_{out} determine the anisotropy of the system. The anisotropy parameter β is given by

$$\beta(r) = 1 - \sigma_t^2(r)/\sigma_r^2(r). \quad (16)$$

If $b_{out} \approx 0$, then $\beta \approx -b_{in}/2$ for $L \ll L_\beta$. Similarly, if $b_{in} \approx 0$, $\beta \approx -b_{out}/2$ for $L \gg L_\beta$.

2.3 Approximate likelihood function

From the DF method, one can perform a statistical analysis to extract the halo parameters and constrain the DM profile based on the full likelihood function discussed in Appendix C. A significant problem with the full likelihood function is its intensive computation requirement. For each star, we are required to perform a multidimensional integration of our DF. In particular, for data sets with hundreds or even thousands of stars, the time to compute the normalized likelihood to perform a Monte Carlo Markov Chain (MCMC) analysis becomes computationally prohibitive. To make the model faster to calculate, we therefore employ an approximation of the full likelihood as described below.

Using the equations in Section 2 and Appendix B, the DF can be used to make predictions of the radial profiles of surface density and velocity dispersion, and a prediction of the (global) VSP. We can compare these predictions to observed values from photometry (in the case of surface brightness) or from spectroscopy (in the cases of velocity dispersion and VSP). The surface density and dispersion observations use binned data, with bins at 8–25 radial locations, typically. The χ^2 for each characteristic is calculated by comparison of the predicted points with the observed values, relative to the uncertainty in the observation:

$$\chi^2 = \frac{(\text{data} - \text{prediction})^2}{\text{uncertainty}^2}. \quad (17)$$

The total χ^2 is then the result of

$$\chi^2_{tot} = \chi^2_{SD} + \chi^2_{disp} + \chi^2_{VSP}, \quad (18)$$

where the subscripts refer to surface density, dispersion and VSP, respectively. We construct the log likelihood according to $\log\mathcal{L} = -\chi^2_{tot}/2$. We perform a Bayesian analysis to derive parameter posteriors. The model employs sampling via the EMCEE package (Foreman-Mackey et al. 2019). Table 1 shows the upper and lower parameter limits for the uniform priors adopted.

As described above, it is necessary to bin the data to make use of this approximation method. For surface density data, the binning is straightforward, because the uncertainty in the measurement is determined by Poisson statistics. However, for the dispersion data, the uncertainty is a combination of spectroscopic measurement uncertainty and the intrinsic random variations of velocities of the stars in each bin. As such, the binning process can make nontrivial differences in the data and resulting inferences. We discuss the binning process in detail in Appendix D. Importantly, we found that using the logarithm of the dispersion resulted in Gaussian distributions of the binned data values, while using the dispersion itself did not. We use $\log_{10}$ velocity dispersion as the variable of interest for χ^2_{disp}.

To perform the multidimensional integrations, we used the VEGAS integration routine (Lepage 1978), which employs adaptive importance sampling and is quite fast. We found that we had to carefully check the convergence of the integrations, as some parameter combinations would cause pathological problems.

Downloaded from https://academic.oup.com/mnras/article/532/4/4157/7718108 by UC - Irvine user on 24 July 2025

2.4 Derived parameters

Once the parameters specifying the DM potential and the DF are inferred we can calculate distributions of surface density and velocity dispersion at a range of radii, and we can derive other quantities of interest such as the half-light radius $r_{1/2}$, the stellar orbital anisotropy β, the DM density at 150 pc ρ_{150}, and the DM halo mass M_{200}.

Since the DF model makes a smooth prediction for surface density, calculation of the half-light radius $r_{1/2}$ is relatively straightforward. The two-dimensional (2D) half light radius $R_{1/2}$ satisfies the equation

$$\frac{\int_0^{R_{1/2}} \Sigma_*(R) R \mathrm{d}R}{\int_0^{R_{\rm max}} \Sigma_*(R) R \mathrm{d}R} = \frac{1}{2}, \tag{19}$$

where $R_{\rm max}$ is the radius of the outermost surface density data point. We verified that using $R_{\rm max}$ rather than an infinite limit did not have a significant effect on the result. This equation can be solved numerically; we then multiply the result by 1.33 to derive the three-dimensional (3D) half-light radius. Wolf et al. (2010) found that the ratio of 1.33 is valid for a variety of stellar profile shapes, and we confirmed this to be a very good approximation for our own mock data sets. We also verified that for the mock data sets, the value obtained by this method was very close to the median radius of the stars in the data set. We use the photometry integration method to calculate the half-light radius posteriors directly from the density predicted by the DF (see equation 1). In what follows, we will also calculate $M(< r_{1/2})$, the mass enclosed within the half-light radius.

3 MOCK DATA MODELLING

Testing the model with mock data allows us to validate our approach and provides an indication of what we can reliably infer via our DF method. We use mock data from the Gaia Challenge spherical data sets (Read et al. 2019a). The Gaia Challenge data were developed for the express purpose of modelling collisionless stellar systems such as dwarf galaxies. We use the spherical versions to match our modelling assumptions. Gaia Challenge employs two types of DM distributions: cuspy ('NFW') and cored. There is also a variety of stellar and anisotropy profile configurations, as we describe below.

3.1 Mock data characteristics

The stellar density profile in the mock data is given by a generalized Hernquist profile (Hernquist 1990; Zhao 1996):

$$\nu_*(r) = \nu_0 \left(\frac{r}{r_*}\right)^{-\gamma_*} \left(1 + \left(\frac{r}{r_*}\right)^2\right)^{\frac{(\gamma_*-5)}{2}}. \tag{20}$$

The parameter γ_* is set to 0.1 for the cored stellar profile and 1.0 for the cuspy stellar profile. The parameter r_* determines how embedded the star population is placed in the DM potential, and was varied among four values: 0.1, 0.25, 0.5, and 1.0 kpc.

The DM potential in the mock data is either 'cored' or 'NFW', as described in Section 2.1. The DM central density ρ_0 is also determined by this choice, with $\rho_0 = 400 \times 10^6 M_\odot \mathrm{kpc}^{-3}$ for the cored case and $\rho_0 = 64 \times 10^6 M_\odot \mathrm{kpc}^{-3}$ for the NFW case. All of the mock data sets have scale radius $r_s = 1$ kpc. The scale velocity v_s is 147.1 km s^{-1} in the cored case and 58.8 km s^{-1} in the NFW case.

The stellar velocity anisotropy profile is also varied among two cases. The orbital anisotropy profile is varied according to an Osipkov–Merrit form (Binney & Tremaine 2008): $\beta(r) = r^2/(r^2 + r_a^2)$, where r_a is the anisotropy radius. The parameter r_a takes the values of either 1 kpc or 10 000 kpc. A value of 1 kpc creates a profile in which β rises from 0 in the centre to 1 in the outer parts, reaching 0.5 at a radius of 1 kpc. A value of $r_a > 10^2$ kpc creates essentially isotropic profiles with $\beta = 0$ everywhere. The mock data sets therefore have $2 \times 4 \times 2 \times 2 = 32$ possible unique configurations.

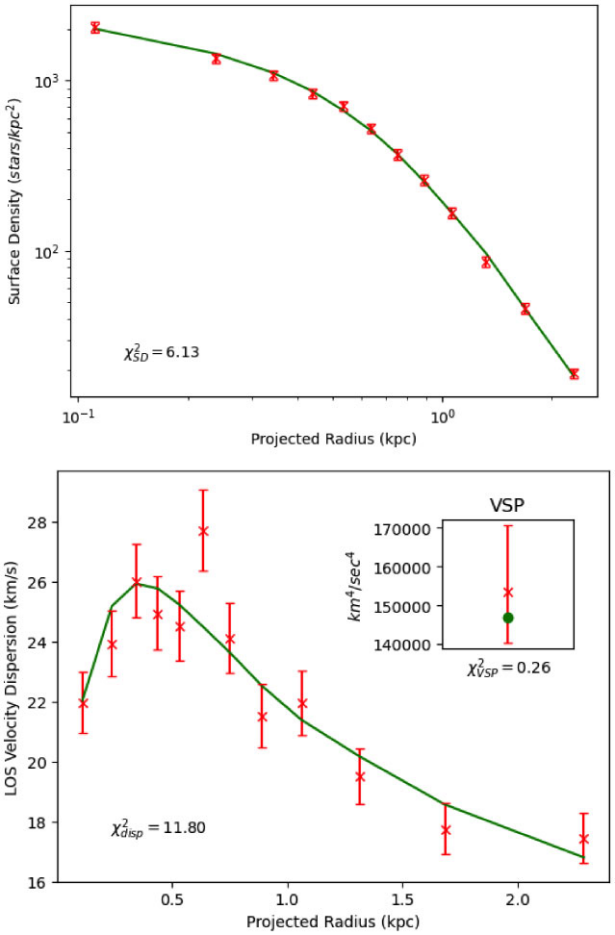

Figure 1. Typical fits to surface density (top), velocity dispersion (bottom), and VSP (bottom, inset), in this case for mock data set 15 (ID bdaO_2677). The data is shown in red and the best-fitting DF solution is shown in green.

The *Gaia* Challenge data sets provide good model validation cases for our model, since certain key parameters are known: r_s, v_s, and w. The data sets contain multiple populations. We selected stars from only one population in each set, and did not include non-member foreground stars. The stars were binned into bins with equal number of stars. We found that the data sets typically had a small fraction of stars with very large orbital radii, which made the outer bins very wide and presented computational challenges. To address this, we opted to exclude the outermost stars from the data sets. Stars farther than 5 half-light radii from the centre were excluded. Less than 10 per cent of the stars from any data set were excluded in this fashion, typically about 5 per cent. To simulate measurement error in the line-of-sight velocities, Gaussian error was added with a standard deviation of 2 km s^{-1}. The data set characteristics are summarized in Appendix O (Table O1).

3.2 Mock data modelling results

The approximate DF model was applied to the 32 mock data sets, the results of which are presented below. Since we wish to simulate that we do not have a priori knowledge of the DM profile, we used

Downloaded from https://academic.oup.com/mnras/article/532/4/4157/7718108 by UC - Irvine user on 24 July 2025

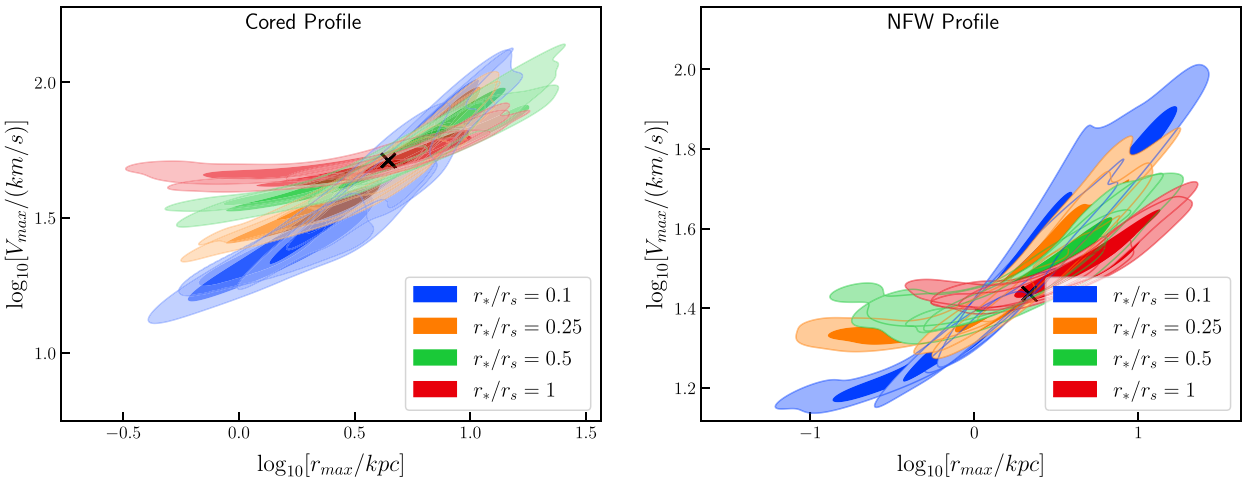

Figure 2. Posteriors for $r_{\rm max}$ versus $V_{\rm max}$ for the 32 mock data sets. Left: 16 Cored profiles. Right: 16 NFW profiles. The 68 per cent and 95 per cent levels are shown, with the 68 per cent level in a darker colour. The black 'x' indicates the true value. The data sets are colour-coded by their embeddedness in the DM halo. There are four sets for each value of embeddedness in each plot, sharing the same colour.

the cNFW profile in the model, in which the core size is a varying parameter. The model found very good fits to the surface density curves, dispersion curves and VSP values in all cases, with χ^2 per degree of freedom ≤ 1.3 for all data sets. A typical fit is shown in Fig. 1.

Fig. 2 shows the posterior inferences in $r_{\rm max}$ versus $V_{\rm max}$ for the 32 mock data sets, with the true value shown as an 'x' near the centres. We used GetDist (Lewis 2019) for two-dimensional plots. The models have a wide diversity of shapes in the $r_{\rm max}$–$V_{\rm max}$ plane, depending on the various profiles for DM density, stellar density, anisotropy, and 'embeddedness' (i.e. the depth of the stars in the DM potential). The figure is colour-coded by embeddedness, and shows how the embeddedness impacts the shape of the posteriors, the degeneracy characteristics between the two parameters, and the inference capability. We found that the highly embedded data sets ($r_*/r_{\rm s} = 0.1$) were the least accurate in their inferences of $r_{\rm max}$ and $V_{\rm max}$, and that tendency carried over into inferences of many other parameters. The model made reliable inferences for the data sets with $r_*/r_{\rm s} >= 0.25$. The reason for the difference is that the highly embedded data sets do not trace the potential near the scale radius $r_{\rm s}$, and so have limited accuracy in that region.

Fig. 3 compares the posterior for the calculated half-light radius to the true value, which is taken to be the median radius of the stars in the data set. The accuracy is very good, with a difference of less than 2 per cent between the median prediction and the true value for all data sets.

The mass within the inferred half-light radius can be determined for the cNFW profile by using the posterior values for $r_{\rm s}$, $v_{\rm s}$, and $r_{\rm c}$. Fig. 4 shows the true and predicted values for the mass within the half-light radius for the mock data sets. The predictions are fairly accurate for the data sets with $r_*/r_{\rm s} \geq 0.25$, i.e. those not deeply embedded in the DM potential. For the data sets with the lowest mass enclosed (and correspondingly very deeply embedded in the DM halo), the model tends to systematically overestimate the mass enclosed.

Predictions for the density at 150 pc as compared to their true values are shown in Fig. 5. The median predictions are generally within 0.3 dex of the true value, with one case near 0.5 dex. In three cases the true values were outside the 95 per cent confidence level of the posterior, all of which were overestimations of the density.

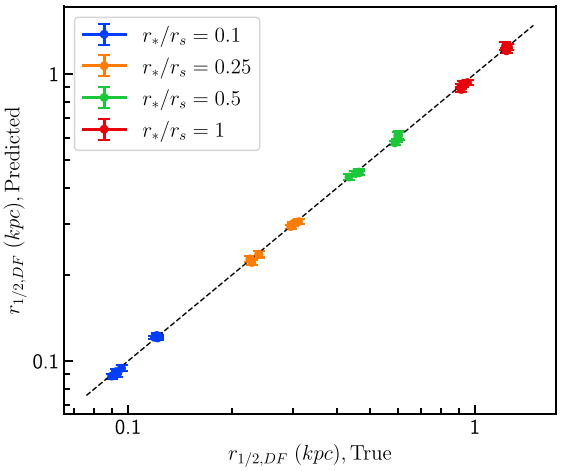

Figure 3. Predicted and true values for the half-light radius for the 32 mock data sets, colour-coded by embeddedness. The predictions are determined from the DF (see equation 1) by calculating and integrating the surface density curve, finding the radius that yields have the total value (see equation 19). The error bars indicate the 68 per cent confidence interval. The true value is taken to be the median radius of the stars in the given data set.

In Appendix E, we show the details for the inference of the core radius for the mock data set, with comparison to the inferences of the observed dSphs. In Appendix F, we provide details of the models prediction performance for the anisotropy parameter β at the half-light radius.

3.3 Summary of model performance with mock data

The approximate DF model makes accurate predictions in the $r_{\rm max}$–$V_{\rm max}$ plane and for half-light radius of the data sets (Figs 2 and 3, respectively). The mass within the half-light radius is predicted well for those data sets that are not too deeply embedded in the DM potential. For the highly embedded data sets, there is a modest tendency to overestimate the mass (Fig. 4). The density at 150 pc (ρ_{150}) is accurate to within 0.5 dex in all cases, and within 0.3 dex in most cases (Fig. 5).

Downloaded from https://academic.oup.com/mnras/article/532/4/4157/7718108 by UC - Irvine user on 24 July 2025

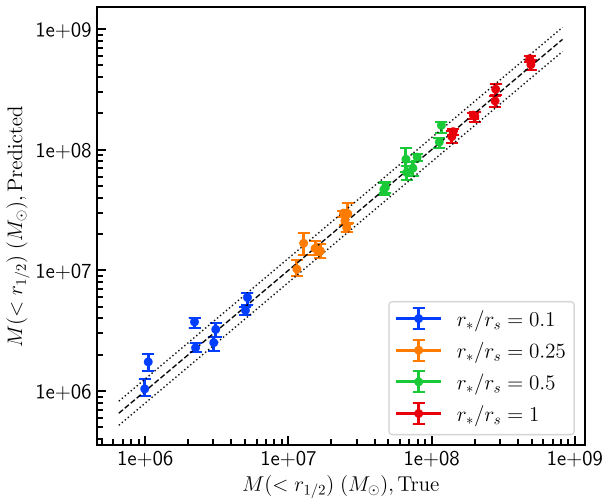

Figure 4. Predicted and true values for the mass within the half-light radius for the 32 mock data sets, colour-coded by their embeddedness in the DM halo. The error bars indicate the 68 per cent confidence interval. The dashed diagonal line indicates equality, with dotted lines indicating ±0.1 dex.

The model shows some ability to distinguish between NFW and cored profiles, which is evident in Fig. E1. The key difference lies in how sharply the posterior gets small at small values of core radius. Our mock data analyses reveals that if the posterior is peaked in core radius, then it is likely a sign of a non-zero core radius if the stars are not too deeply embedded. For deeply embedded stellar profiles, it seems difficult to make this distinction. We also looked at the predictions for $\beta(r_{1/2})$ and found them to be of limited accuracy. The inferences become progressively less robust for cases that are deeply embedded and that have rising β profiles (Fig. F1).

4 BRIGHT DWARF SPHEROIDAL MODELS: CONSTRAINTS ON THE HALO PARAMETERS

We selected as our sample the eight classical dSphs of the MW, plus Canes Venatici I, as shown in Table 2. The results from applying the DF model are described here. We use cNFW as the DM profile, as it is the most general of our profiles. For the distance to each target, we adopt the median value of the distance shown in the second column of Table 2. We use surface density data from Muñoz et al. (2018). Dispersion data is from Mateo, Olszewski & Walker (2008), Walker et al. (2009), Walker, Olszewski & Mateo (2015), Spencer et al. (2017), and Walker (private communication). VSP data is from Kaplinghat et al. (2019). The results from the analysis are discussed here.

4.1 How surface density and velocity data constrain r_{max}, V_{max}, and DM density

Here we ask: How do the various components of the data set put constraints on key parameters such as r_{max}, V_{max}, and (indirectly) the DM density ρ_{150}? The parameters r_{max} and V_{max} are related in a straightforward way to the scale radius r_s and the velocity scale v_s, so let us turn our attention to these. The prediction for surface density is given by equations (1), (4), and (6), which in turn depends on the potential, which is defined in terms of v_s. Therefore, at first blush, surface density appears to depend intimately on v_s. However, it can be demonstrated numerically that there is very little dependence. This can be explained as follows. Assume for the moment that a particle is not near the tidal limit, so we can ignore the term $(\Phi_{lim} - E)^e$ in equation (12). Note that the energy of a particle is given by $E(r, v) = \Phi(r) + \frac{1}{2}v^2$. For stars near the centre of the galaxy, the second term is dominates, and $E \propto v^2$, independent of v_s. For stars far from the centre (but not near the tidal limit), the potential term dominates, and $E \propto \Phi(r) \propto v_s^2$. The energy term of the DF is given by equation (12). If $E \ll \Phi_{lim}$, then $h(E) \propto E^p$, where the exponent p takes a value $p \approx a$ for small energies, with $p \approx a + d$ at large energies. Since the star is far from the centre, its potential energy will be large and the star will likely be in the region $p \approx a + d$. Recall that d must be negative, and in fact all the mock data and observed dSph models prefer solutions with $(a + d) < 0$. This then gives the energy function $h(E) \propto v_s^{2(a+d)} + \frac{1}{2}v^2$. The negative exponent in the first term causes that term to be small compared to the second, and again the result is insensitive to v_s. If a particle is near the tidal limit, the term $(\Phi_{lim} - E)^e$ will be small by definition, and there will be very few stars in that area of parameter space.

To illustrate the constraining power of the various χ^2 components of the DF model (ref. equation 18) we examine the results of the Draco and Fornax dwarfs as typical examples. Fig. 6 shows how the three components of χ^2 put restrictions on r_{max} and V_{max} for those dSphs. The surface density data strongly constrains r_{max} but has virtually no constraining power for V_{max}, as expected from the above discussion. This also matches the intuitive notion that without stellar velocity information it is difficult to characterize the velocity scale of the DM potential. The velocity dispersion grossly constrains both r_{max} and V_{max}, but it is the combination of surface density and dispersion data that results in a tight constraint in the (r_{max}, V_{max}) plane. The fourth-order moment (VSP) adds a modest additional constraint (see also Fig. 9). The constraint features illustrated here for Draco and Fornax are very similar for the other dSphs as well.

It is also interesting to examine how the constraints on r_{max} and V_{max} translate to ρ_{150} (the DM density at 150 pc) and $M(< r_{1/2})$ (the mass within the half-light radius). Fig. 7 shows the dependence of those parameters on r_{max} and V_{max} for the Draco and Fornax dSphs. It illustrates that the lines of constant ρ_{150} and $M(< r_{1/2})$ for these models tend to run parallel to the long axis of the posterior, which allows a strong constraint on those parameters even given the wide range of possible solutions in the (r_{max}, V_{max}) plane.

4.2 Inference of mass within key radii: comparisons with dispersion-based mass estimators

It is informative to examine the inferences for the mass of the dSphs enclosed within key radii, as such inferences can be readily compared with dispersion-based estimators. These key radii are the half-light radius $(r_{1/2})$ and $\mathcal{O}(1)$ multiples of it, which are good places to measure the mass and density of DM, since there is usually good luminosity and dispersion data there, and the inferred density can tell us something about the cores of the subject haloes. Wolf et al. (2010) used the luminosity-weighted LOS velocity dispersion to derive an estimate for the mass within the half-light radius $(r_{1/2})$ that was relatively immune to the mass-anisotropy degeneracy problem. Other authors followed suit, notably Errani et al. (2018), who found that the mass enclosed within 1.8 $r_{1/2}$ was even better insulated from mass-anisotropy fluctuations. Note that as described more fully in Section 4.4, we use the spherical radius, and therefore convert the results of other authors from elliptical radius to its sphericalized equivalent.

In Fig. 8, we compare the mass enclosed within 1.8 $r_{1/2}$, corresponding to the mass estimator of Errani et al. (2018), and also the mass enclosed within $r_{1/2}$, corresponding to the mass estimator

Downloaded from https://academic.oup.com/mnras/article/532/4/4157/7718108 by UC - Irvine user on 24 July 2025

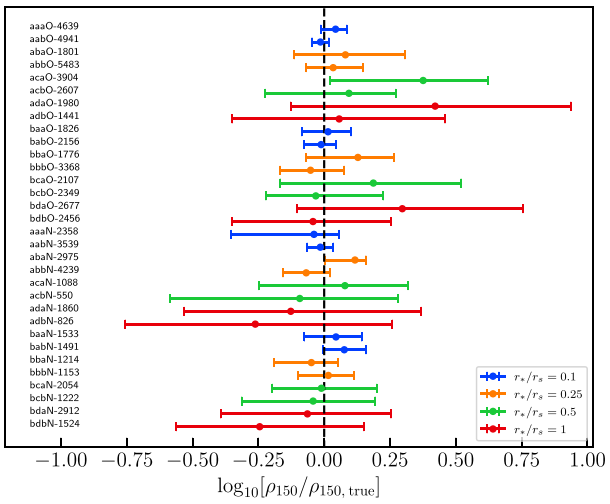

Figure 5. Predicted and true values for DM density at 150 pc for the 32 mock data sets, colour-coded by embeddedness. The error bars indicate the 95 per cent confidence interval. The labels for each data set are shown on the left and correspond to those in Table O1.

of Wolf et al. (2010), for the observed dwarfs. The DF method predicts masses that are fairly consistent with those predicted by the mass estimator methods. The only substantial disagreement is for the Fornax dSph, where our inference of $M(< 1.8\ r_{1/2})$ is somewhat higher than that derived by Errani et al. (2018), although our inference for $M(< r_{1/2})$ is consistent with that of Wolf et al. (2010).

4.3 Inferences for r_{max} and V_{max}

Predictions for r_{max} and V_{max} for the observed sample are presented in Fig. 9. The two parameters show strong positive correlation. Because the halo scale density $\rho_s \propto r_s^2/v_s^2$, this type of degeneracy is approximately along lines of constant density, so that the density is relatively well constrained, as discussed previously. To demonstrate the effect of the VSP, the posteriors that result from excluding the VSP component in the analysis are shown in the figure with dotted black lines. The VSP does indeed add some predictive power, making the posteriors somewhat smaller and in some cases shifting them modestly.

In Fig. 9, the black triangles show the 10 most massive subhaloes from the fiducial Phat Elvis halo (1107, which has a halo mass of $8.9 \times 10^{11} \mathrm{M}_\odot$) and restricted to those subhaloes that are more than 50 kpc from the centre. We chose this as our fiducial halo because it is closest in mass to the light MW model used by Battaglia et al. (2022).

If we use a more massive Phat Elvis halo for fiducial comparison, the triangles of the 10 largest subhaloes will tend to shift upward and to the right (i.e. they will have larger r_{max} and V_{max}). The TBTF problem then becomes even more pronounced, i.e. the simulation predicts a large number of dense and massive subhaloes, inconsistent with what is seen in the MW. Moreover, such a choice of fiducial halo mass for the Phat Elvis simulation would be inconsistent with the MW models used by Battaglia et al. (2022) in our analysis. The simulated V_{max} values would be systematically larger than those we infer for the MW satellites. (Comparing the r_{max} and V_{max} inferences for the bright MW dwarfs to those of all of the subhaloes in the Phat Elvis suite of simulations, the results are similar: they are generally consistent in V_{max}, but the inferences for the r_{max} of the bright MW dwarfs are generally higher than those in Phat Elvis.)

Since our sample represents the brightest 9 MW dSphs, one would expect these to be of comparable V_{max} to those in the Phat Elvis simulation. This is generally true; the posteriors for Fornax and Sculptor are centred near the top of the range and indeed extend above the top. The V_{max} posteriors for Draco, Carina, and Ursa Minor straddle the middle range, while the others are closer to the bottom and indeed extend beyond the lowest V_{max} of the 10 most massive subhaloes. In contrast, the r_{max} posteriors for many of the 9 bright MW dSphs seem to be systematically at larger values than those of the Phat Elvis subhaloes, especially Draco, Fornax, Carina, and Sculptor. This might be expected if the haloes are cored, as may be indicated for Fornax and perhaps Carina. The posteriors of the MW dSphs all have the familiar degeneracy between r_{max} and V_{max} (i.e. they are positively correlated), very similar to that observed in the mock data in Fig. 2. We note that, in the mock data tests, there was no systematic overprediction of r_{max}. This also presents itself as a generally lower central density inference of the subhaloes in the sample as compared to the simulated subhaloes, as can be seen in Section 7.

Table 2. The Dwarf Galaxy Sample. Adopted distance, 2D half-light radius $R_{1/2}$ and V-band magnitude M_V are from Simon (2019). Ellipticity ϵ and position angle θ are from Muñoz et al. (2018). Centre coordinates are from The NASA/IPAC Extragalactic Database (NED). Pericenter distances are from the light MW model (no LMC) of Battaglia et al. (2022). Stellar masses M_* are from McConnachie (2012).

Name	Adopted distance (kpc)	Centre RA (deg)	Centre dec. (deg)	$R_{1/2}$ (pc)	ϵ	θ (deg)	Pericenter (kpc)	M_V	M_* ($10^6 \mathrm{M}_\odot$)
Draco	82.0	260.051625	57.915361	237 ± 17	0.29	87	$51.7^{+4.1}_{-6.1}$	$-8.88^{+0.05}_{-0.05}$	0.29
Fornax	139.0	39.997200	−34.449187	792 ± 18	0.29	45	89^{+31}_{-26}	$-13.34^{+0.14}_{-0.14}$	20
Carina	106.0	100.402888	−50.966196	311 ± 15	0.36	60	$106.7^{+6.4}_{-5.4}$	$-9.45^{+0.05}_{-0.05}$	0.38
CnV I	211.0	202.014583	33.555833	437 ± 18	0.44	80	$68.09^{+71.49}_{-42.17}$	$-8.73^{+0.06}_{-0.06}$	0.23
Leo I	254.0	152.117083	12.306389	270 ± 17	0.30	78	$46.53^{+30.50}_{-26.54}$	$-11.78^{+0.28}_{-0.28}$	5.5
Leo II	233.0	168.370000	22.151667	171 ± 10	0.07	38	$115.55^{+88.35}_{-58.87}$	$-9.74^{+0.04}_{-0.04}$	0.74
Sculptor	86.0	15.038984	−33.709029	279 ± 16	0.33	92	$63.7^{+4.5}_{-3.1}$	$-10.82^{+0.14}_{-0.14}$	2.3
Sextans	95.0	153.262319	−1.614602	456 ± 15	0.30	57	$74.45^{+4.38}_{-5.68}$	$-8.94^{+0.06}_{-0.06}$	0.44
Ursa Minor	76.0	227.285379	67.222605	405 ± 21	0.55	50	$48.9^{+3.4}_{-3.3}$	$-9.03^{+0.05}_{-0.05}$	0.29

Downloaded from https://academic.oup.com/mnras/article/532/4/4157/7718108 by UC - Irvine user on 24 July 2025

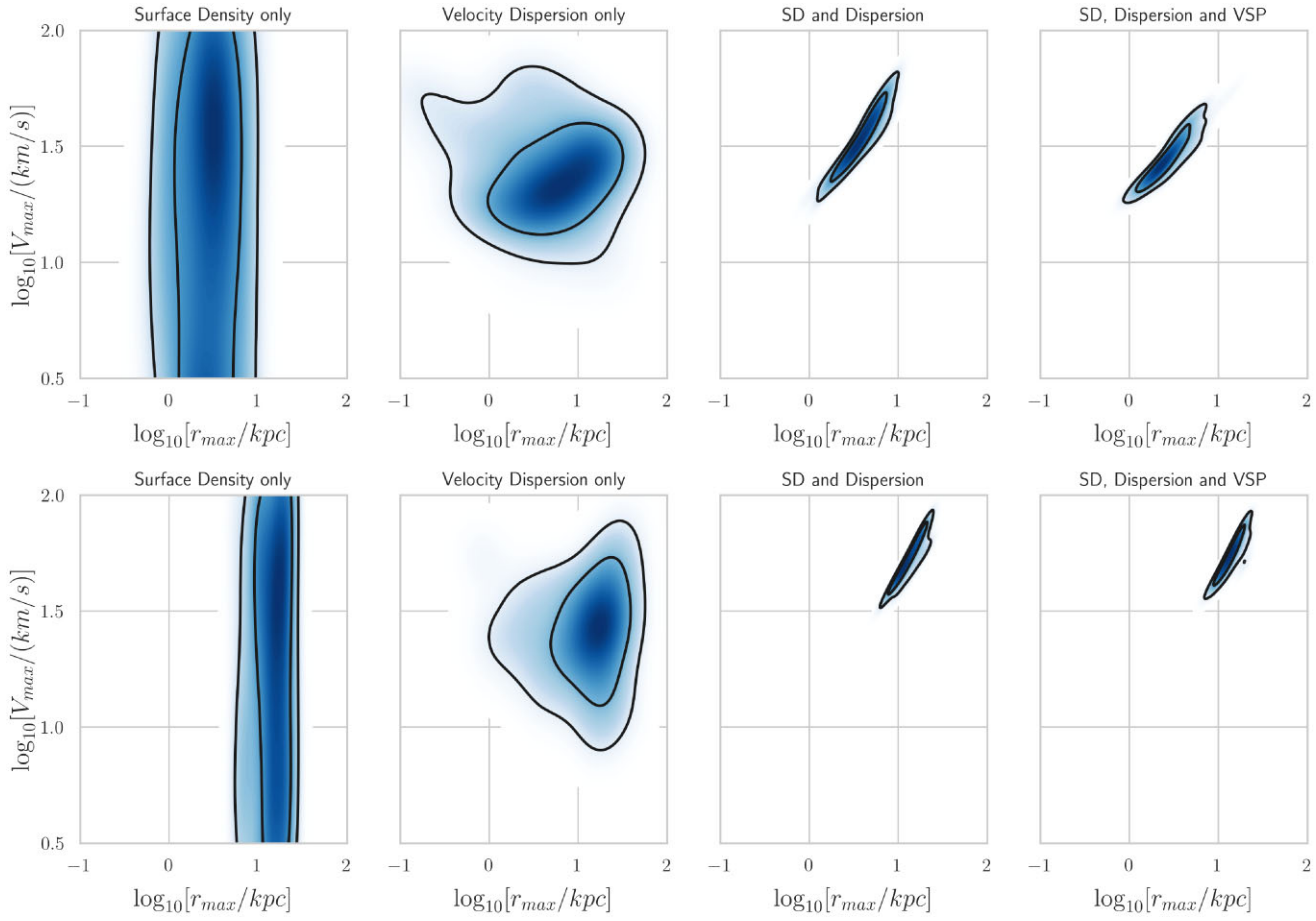

Figure 6. Constraints on $r_{\rm max}$ and $V_{\rm max}$ from the χ^2 components of surface density, velocity dispersion, and VSP. *Top panel:* Draco. *Bottom panel:* Fornax. The black contour lines indicate the 68 per cent and 95 per cent confidence levels. The first column shows the posterior distribution when only surface density is used in χ^2. The second column corresponds to only using velocity dispersion in χ^2. The third column corresponds to using surface density and velocity dispersion, but not the VSP. The fourth column corresponds to using all three components in the calculation of χ^2.

4.4 Half-light radius of the observed sample

The half-light radius posteriors for the observed sample are shown in Table 3. Comparison with previous authors is not straightforward, because of fundamentally different approaches in computation. We compare to Muñoz et al. (2018), who fit a Sersic profile to 2D data maps of the dwarfs. We multiply the Muñoz et al. (2018) result by the axis ratio of its elliptical profile, $\sqrt{1-\epsilon}$, to convert from elliptical radius to a spherical one. The data used for our models is a 1-dimensional equivalent of their data, also adjusted for ellipticity. We also show the $R_{1/2}$ resulting from a 2-parameter Plummer profile (Plummer 1911) fit of our input data. The DF approach does not rely on any profile shape; we simply find the radius that encloses half of the stars. As can be seen in the table, there can be substantial differences between the various methods. One notable difference is in Leo I, for which the DF predicts a median value of 0.315 kpc while the Plummer fit to the same data yields 0.308 kpc, and Muñoz et al. (2018) find 0.204 kpc. Possible reasons for the difference are (a) the surface density map for Leo I is quite boxy, with ellipticity that appears to change with position angle, and (b) the surface density plateaus considerably at larger radii, making it a poor fit for most parametrized profiles. We note that Read et al. (2019b) used Jeans analysis combined with virial shape parameters to examine these objects and found 2D half-light radii of 0.298 kpc and 0.194 kpc for Leo I and Leo II, respectively, consistent with our findings.

Fig. 10 shows 2D posteriors for the half-light radius of the observed sample versus the mass enclosed within that radius. The distribution of masses enclosed within the half-light radii seems to split into two groups. Fornax stands out with the largest half-light radius and largest mass enclosed; however, it is in the group with the lowest average density within the half-light radius, accompanied by Carina and Sextans. At the other end of the spectrum are Draco and Leo II, which are the most compact, enclose the least mass but have the highest density within $r_{1/2}$.

We compare the results of our DF model to those of other approaches in Section 6 and find that our inferences for $r_{\rm max}$, $V_{\rm max}$, and ρ_{150} are generally consistent with the other methods, with a few exceptions. The model inferences for core parameter ($c = r_{\rm c}/r_{\rm s}$), anisotropy (β), and embeddedness ($r_{1/2}/r_{\rm s}$) are discussed in Appendices G, H, and I, respectively. As the MW has strong tidal forces, we investigate the possible impacts of tidal truncation in Appendix N, and conclude that the likely impacts on our inferences for $r_{\rm max}$, $V_{\rm max}$, and ρ_{150} are small.

5 THE DIVERSITY OF DSPHS

A convincing theory of DM will have to explain the diverse density profiles seen in the MW's dwarf spheroidal galaxies, with Draco and Fornax at the extreme ends. We find Draco to be the smallest

Downloaded from https://academic.oup.com/mnras/article/532/4/4157/7718108 by UC - Irvine user on 24 July 2025

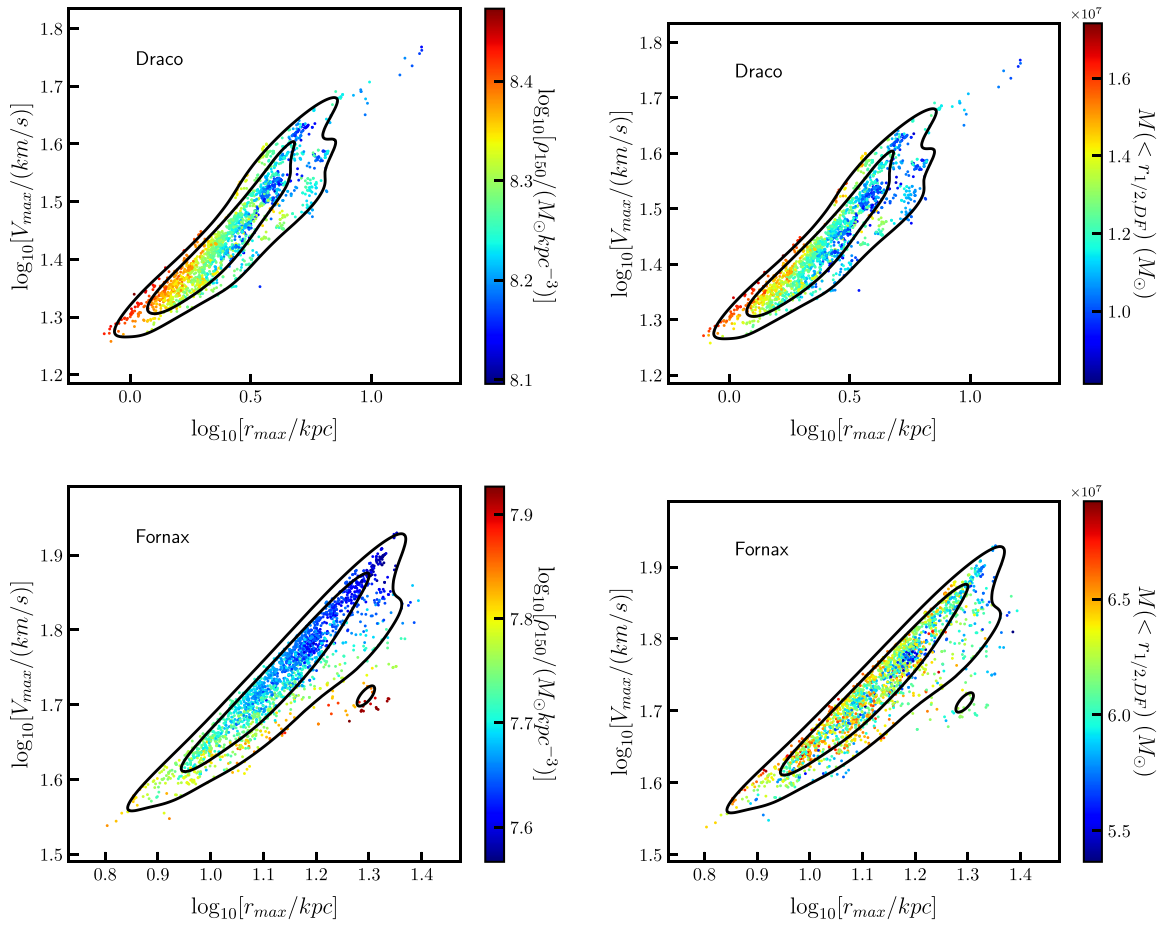

Figure 7. The $r_{\rm max}$, $V_{\rm max}$ plane for Draco (*top row*), and Fornax (*bottom row*). The black contour lines indicate the 68 per cent and 95 per cent confidence levels. *Left Column*: ρ_{150} shown in colour. *Right Column*: $M(< r_{1/2})$ shown in colour. Lines of constant ρ_{150} and $M(< r_{1/2})$ are roughly parallel to the long axis of the posterior, allowing relatively strong constraints on both parameters.

and densest of the observed sample, with 3D half-light radius approximately 260 pc, while Fornax is the largest and among the least dense, with half-light radius of approximately 760 pc (see Section 4.4 for a full discussion.) Carina looks similar to Fornax, though not as extreme, with a low DM core density and preference for a relatively large core. While it is difficult to predict the core radius from our method accurately, the shape of the posteriors for Carina and Fornax are clearly inconsistent with a cuspy profile (Fig. E2). We refer the reader to Appendix E for more details on posteriors for the core radii. Conversely, Leo I and Leo II prefer small core radii or cuspy profiles, and high ρ_{150}. The posteriors of Draco and Sculptor are consistent with those dSphs being hosted by cored dark matter haloes, but with core sizes smaller than those of Fornax and Carina. For all dSphs, the inferred core radii are smaller than or comparable to the respective half-light radii. We note that core collapse can occur in SIDM haloes, with a time scale sensitive to the (possibly velocity-dependent) cross-section per unit mass (Elbert et al. 2015; Shah & Adhikari 2023; Zeng et al. 2023; Yang, Nadler & Yu 2023), although we do not explore core collapse in this work.

Fig. 11 shows the this work's DF model inferences for the DM density as a function of radius compared to the Jeans analysis inferences of the cored isothermal and NFW cases of Kaplinghat et al. (2019). Noted on the plots are lines for logarithmic slopes of 0 and -1, corresponding to cored and cuspy DM distributions, respectively. For both dwarfs, the density profiles are similar to the cored isothermal cases of Kaplinghat et al. (2019), showing a cusp (or a very small core) in Draco and a core (or a very mild cusp) in Fornax. Cuspy DM haloes are found in standard CDM only simulations (Navarro, Frenk & White 1996), whereas cored DM haloes require either non-gravitational DM microphysics such as self-interactions, or explanations via baryonic mechanisms such as supernova feedback (Penarrubia, Navarro & McConnachie 2008; Vogelsberger, Zavala & Loeb 2012; Rocha et al. 2013; Di Cintio et al. 2014; Vogelsberger et al. 2014; Elbert et al. 2015; Sawala et al. 2016; Bullock & Boylan-Kolchin 2017; Benítez-Llambay et al. 2019; Despali et al. 2022). Note that while most of the MW dSphs are highly DM dominated, Fornax has a stellar mass of approximately $2 \times 10^7 M_\odot$ (see Table 2), by far the largest in the sample, amounting to a few per cent of the dynamical mass. This may suggest that baryonic effects could be responsible for the cored profile in Fornax. Further comparisons with prior works are noted in Battaglia & Nipoti (2022).

6 COMPARING THE DF METHOD TO OTHER METHODS

In Fig. 12, we compare the $r_{\rm max}$ and $V_{\rm max}$ inferences to those of Kaplinghat et al. (2019) and Errani et al. (2018). Kaplinghat et al. (2019) used Jeans analysis for their inference and also utilized the

Downloaded from https://academic.oup.com/mnras/article/532/4/4157/7718108 by UC - Irvine user on 24 July 2025

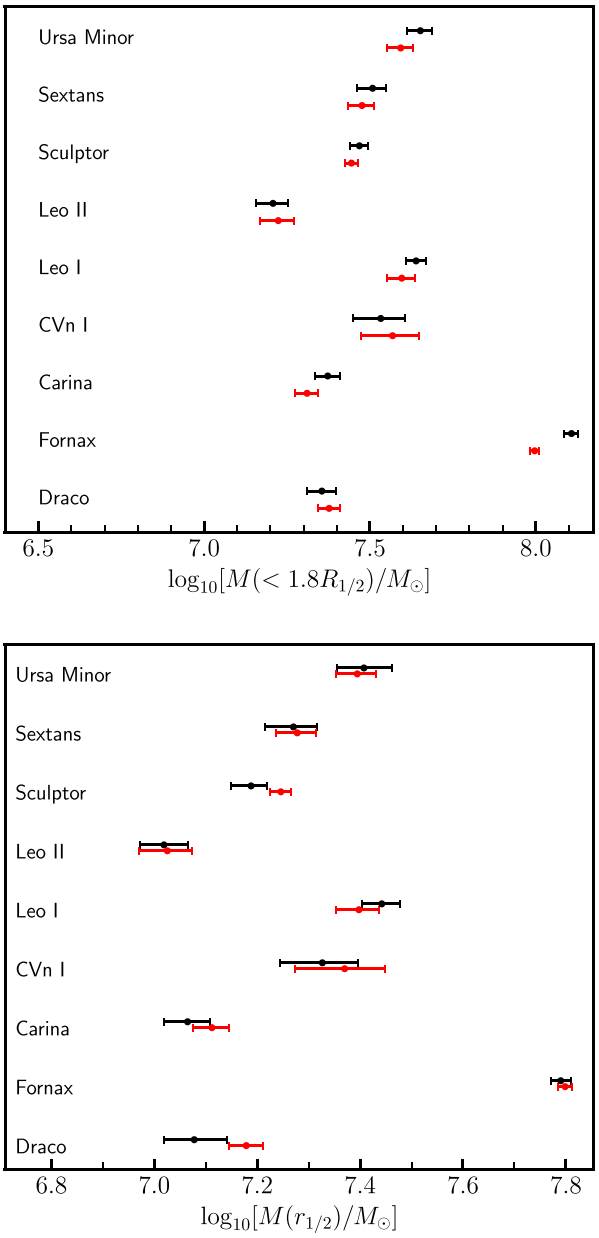

Figure 8. Comparison of mass estimators from Errani, Peñarrubia & Walker (2018) and Wolf et al. (2010), which utilize luminosity-weighted velocity dispersion, with the results of this work. The result of the DF method from this work are shown in black. *Top:*$\log_{10}[M(< 1.8r_{1/2})/\mathrm{M}_\odot]$, which is the mass estimator of Errani et al. (2018), shown in red. *Bottom:*$\log_{10}[M(< r_{1/2})/\mathrm{M}_\odot]$, which is the mass estimator of Wolf et al. (2010), shown in red.

VSP. They analysed two cases, one for an NFW profile and a second for a cored isothermal profile. Their results are similar to ours, with inferences from the DF and Jeans methods generally overlapping at their 1σ boundaries. The exceptions are for the $V_{\rm max}$ of Carina, Fornax and Draco, and the $r_{\rm max}$ of Fornax. In those, the DF predictions are larger than those from either profile in the Jeans analysis. The two methods have fundamental differences, namely the different modelling of stellar velocity anisotropy and the assumption of a Plummer surface density profile in the Jeans analysis. Our analysis is more general, as the DF approach accommodates a wide variety of distributions for the stellar population. Possible other reasons for the differences could include (1) different prior assumptions between the two methods and (2) for Fornax, that Kaplinghat et al. (2019) accounted for the stellar mass in the potential, in contrast to this work where we have assumed that the stars are massless tracers of the DM potential. We note that for Fornax, we infer $V_{\rm max} > 45$ km s^{-1} at the 1σ level, substantially higher than either of the Jeans analysis cases.

Errani et al. (2018) derived $r_{\rm max}$ and $V_{\rm max}$ by using the observed kinematics of the dwarfs in combination with a population of simulated subhaloes. Errani et al. (2018) used spherical Plummer profiles for the stellar population. For the DM, they used an NFW profile for their cuspy case. For the cored case, they use

$$\rho(r) = \rho_{\rm s}[1 + (r/r_{\rm s})]^{-5}. \quad (21)$$

The inferences from their cuspy and cored cases can be seen in the orange solid lines and orange dashed lines, respectively, of Fig. 12. Our results are consistent with their cuspy cases, except for Carina and Fornax (and, to a lesser extent, Sextans), where their cored case is a better match.

Table 4 and Fig. 13 compare our findings for ρ_{150} to those of Read et al. (2019b), Kaplinghat et al. (2019), and Hayashi et al. (2020). The results are generally comparable within errors. However, our finding for Carina at $4.7^{+0.9}_{-0.7}\mathrm{M}_\odot$ kpc^{-3} is lower than the others, inconsistent with that of Read et al. (2019b), Hayashi et al. (2020) and the NFW case of Kaplinghat et al. (2019), but compatible with their isothermal case. Our finding is consistent with a cored halo, as is suggested by the posterior for $r_{\rm core}$ (see Fig. E1). We checked to see if excluding large values of c in the cNFW profile would change this inference significantly, but it does not; we found that if the core parameter is restricted so that $0 < c < 1$, the inference for ρ_{150} increases only approximately 0.1 dex.

7 INCONSISTENCY WITH SIMULATION: DENSITY AT 150 PC VERSUS PERICENTER DISTANCE

An anticorrelation between the density at 150 pc (ρ_{150}) and the orbital pericenter distance ($r_{\rm p}$) for the MW dSphs was noted in Kaplinghat et al. (2019), and is the subject of some debate (Hayashi et al. 2020; Cardona-Barrero et al. 2023). A closely related and perhaps more cogent question is whether the ρ_{150}–$r_{\rm p}$ relationship is consistent with N-body simulations of MW analogues, for if they are not, it is a challenge for ΛCDM that could require more sophisticated physics in such simulations, or could point to new physics such as DM self-interaction Correa (2021).

For orbital pericenter data we turn to the work of Battaglia et al. (2022), which calculated the pericenter distances for the MW dwarfs using *Gaia* data release 3 and which attempts to account for the impact of the Large Magellanic Cloud (LMC) on the potential and orbits. They examined two MW mass scenarios, a 'light' version with mass 10^{12} M$_\odot$ and a 'heavy' version with mass 1.6×10^{12} M$_\odot$. They also examine the light version without the LMC. We use their light model (both with and without the LMC) for our comparisons, although we check the result against the heavy model in Appendix L. Note that the pericenter distances quoted are those of the last calculated pericenter passages, although the orbit integration calculations are carried backward in time to approximately 8 Gyr ago. Prior to that study, Patel et al. (2020) published an analysis accounting for the effect of the LMC in five of the MW dwarf pericenters: Carina, Draco, Fornax, Sculptor and Ursa Minor. Subsequent to our main analysis, another study was published that attempts to account for the LMC in their pericenter projections: Pace, Erkal & Li (2022). The

Downloaded from https://academic.oup.com/mnras/article/532/4/4157/7718108 by UC - Irvine user on 24 July 2025

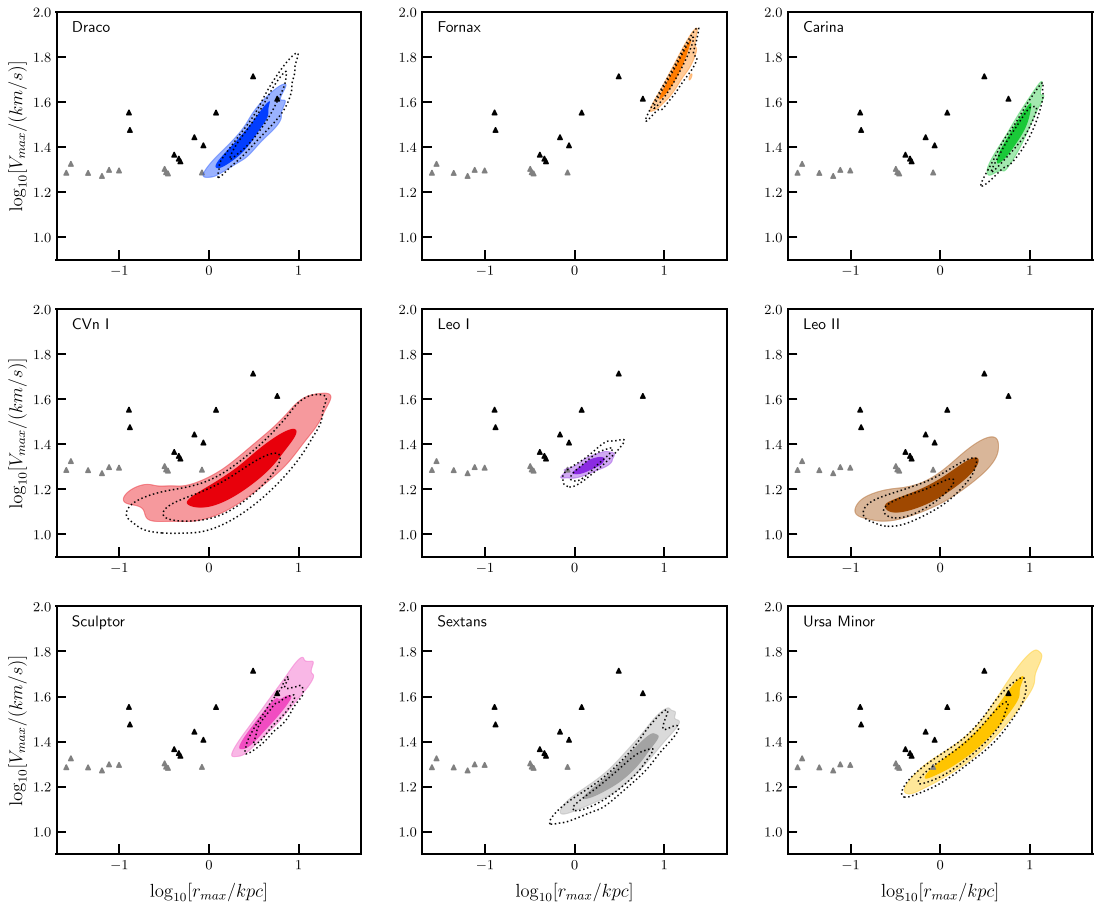

Figure 9. Posterior inferences for $r_{\rm max}$ versus $V_{\rm max}$ for the observed sample. The 68 per cent and 95 per cent levels are shown, with the 68 per cent level in a darker colour. The dotted black lines indicate the posterior result without the VSP χ^2 component. The black triangles represent the 10 subhaloes from the Phat Elvis simulation (halo 1107, with disc) that are more than 50 kpc from the centre of the halo and have the highest $V_{\rm max}$. The grey triangles show the subhaloes with 10th through 20th highest $V_{\rm max}$.

Table 3. Comparison of 2D projected half-light radius ($R_{1/2}$), in kpc. The 'DF' column is the $r_{1/2}$ posterior result from the DF, converted to 2D projected $R_{1/2}$ by dividing by 1.33. The 'Plummer Fit' is the result from the best fitting 2-parameter Plummer profile, as applied to the (one-dimensional) sphericalized surface density data. The rightmost column is the half-light radius reported by Muñoz et al. (2018) for a Sersic profile fit to 2D surface density maps, sphericalized as described in the text.

dSph name	DF	Plummer fit	Muñoz et al. (2018)
Draco	0.197 ± 0.003	0.235	0.183
Fornax	0.574 ± 0.004	0.688	0.668
Carina	0.327 ± 0.003	0.344	0.277
CVn I	0.381 ± 0.010	0.445	0.357
Leo I	0.315 ± 0.004	0.308	0.204
Leo II	0.200 ± 0.002	0.206	0.162
Sculptor	0.243 ± 0.002	0.276	0.244
Sextans	0.397 ± 0.005	0.470	0.370
Ursa minor	0.299 ± 0.004	0.325	0.257

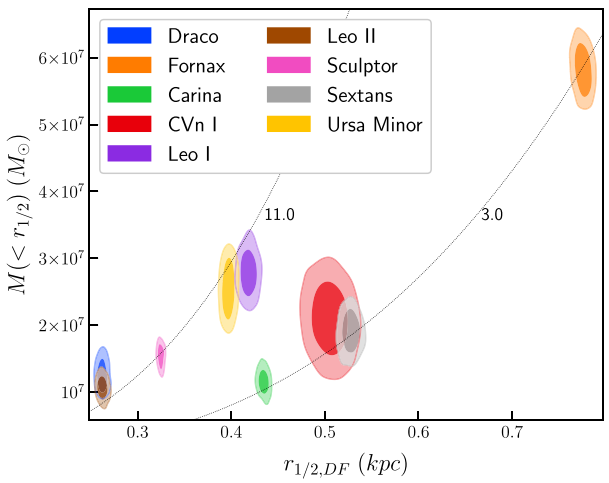

Figure 10. Posteriors for the half-light radius and mass within that radius for the observed sample. The 68 per cent and 95 per cent levels are shown, with the 68 per cent level in a darker colour. Isodensity contours are shown as dotted lines, with the density value indicated, in units of $10^7\ {\rm M}_\odot\ {\rm kpc}^{-3}$.

various sources for pericenter are compared in Appendix L. Although there are some differences, there is a fair amount of consistency between them after considering their stated uncertainties. D'Souza & Bell (2022) showed that care must be taken when back-integrating the orbits of MW satellites in parametric potentials, and that the

Downloaded from https://academic.oup.com/mnras/article/532/4/4157/7718108 by UC - Irvine user on 24 July 2025

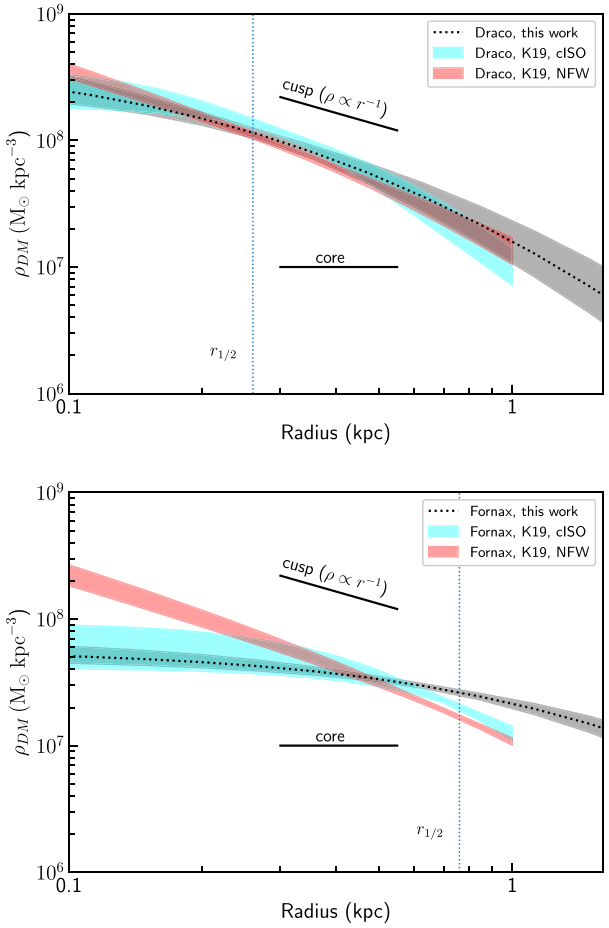

Figure 11. Inferences for dark matter density versus radius compared to those of Kaplinghat et al. (2019), for Draco (top panel) and Fornax (bottom panel). The shaded bands indicate the 68 per cent confidence interval. The DF inferred (3D) half-light radius is shown as a dotted vertical line.

LMC does have a substantial effect on the projection, a result that is underlined by the differences in the pericenters obtained in the with-LMC and without-LMC models of Battaglia et al. (2022).

The posteriors for the density at 150 pc (ρ_{150}) for the observed sample are shown in Fig. 14, plotted against the orbital pericenter distance (r_p) of each dwarf, in the left panel without considering the LMC, and in the right panel accounting for the LMC. In both figures, there is a clear anticorrelation between the pericenter distance and the density at 150 pc, as was also noted in Kaplinghat et al. (2019); however, the correlation appears somewhat stronger in that work than it does here. The best-fitting line is shown in dashed red in Fig. 14. We infer that the slope of the best fit line is negative, as detailed in Appendix J. We examined this correlation using a variety of alternative sources for pericenter distances, including Fritz et al. (2018), Patel et al. (2020), and Battaglia et al. (2022) (including the 'heavy' MW variations in Patel et al. (2020) and Battaglia et al. (2022); see Appendix L), and also using Read et al. (2019b) data for ρ_{150} rather than our own. The negative correlation between ρ_{150} and pericenter distance persists in all cases. Hayashi et al. (2020) also found an anticorrelation in their work, although their analysis is not as directly comparable because they use an axisymmetric model for their DM halo, leading to more parameters, more degrees of freedom and large uncertainties in parameter inferences. We have used more recent pericenter data than Kaplinghat et al. (2019) and Hayashi et al. (2020). Cardona-Barrero et al. (2023) examines the correlation in some detail for various data sets, and concludes that the anticorrelation is statistically significant at the 3σ level in only a minority of the various combinations. We discuss their comparison in Appendix L.

For comparison with simulation, we turn to the Phat ELVIS simulations (Kelley et al. 2019), a suite of 12 MW-similar haloes with a disk potential, with masses ranging from $7.1 \times 10^{11} M_\odot$ to $1.95 \times 10^{12} M_\odot$. We use their host halo 1107 for our fiducial comparison, which has a mass of $8.88 \times 10^{11} M_\odot$ [the most similar to the light MW model of Battaglia et al. (2022)], but the results are similar for all 12 host haloes (see Appendix K and Fig. K1). The Phat ELVIS simulation did not attempt to account for the effect of such a large satellite as the LMC, so we present comparisons to both the with- and without-LMC models of Battaglia et al. (2022). Shown in Fig. 14 are the 20 subhaloes in the fiducial host halo with the largest V_{peak} (i.e. the largest V_{max} since their infall) that are currently located more than 50 kpc from galactic center, plotted as black and grey circles. There is a clear discrepancy between the simulated and observed haloes, with the simulated haloes at distances greater than 50 kpc exhibiting a positive correlation between ρ_{150} and pericenter. Note that significant negative correlation between ρ_{150} and pericenter is not a requirement for inconsistency here; even an absence of correlation would appear to be inconsistent with the simulated haloes. We note that Hayashi et al. (2020) did a similar analysis but did not restrict their regression to the largest haloes. Smaller haloes tend to show some survivor bias in that less dense subhaloes are more likely to be disrupted by tides, thus removing haloes from the lower left of the plot, as described in Kaplinghat et al. (2019). Artificial numerical disruption of subhaloes on orbits with small pericenters is also a crucial factor to consider here but the most massive subhaloes should be the ones that are the least impacted by this (Diemand, Kuhlen & Madau 2007; D'Souza & Bell 2022). In addition, if we choose to populate the bright MW dwarfs in lower mass subhaloes, then we will be left with an even more pronounced too-big-to-fail problem. For these reasons, we restrict the analysis to the 20 largest subhaloes. Our results show that the density-pericenter data still remains a challenge that be met by galaxy formation models. In this regard, it is useful to note that the orbital radii and densities are expected to have an anticorrelation in SIDM models with large cross-sections (Nishikawa, Boddy & Kaplinghat 2020; Sameie et al. 2020; Correa 2021; Yang et al. 2023), and that baryonic effects may also indirectly impact this (Read et al. 2019b).

One might wonder if using the heavier MW models would alter the conclusion, but it does not (see Appendix L, Fig. L1). The pericenter projections of Patel et al. (2020), Battaglia et al. (2022), and Pace et al. (2022) are the current state-of-the-art for the MW dSph pericenters but rely on static, axisymmetric potentials for the MW. We look for possible biases in this approach in Appendix M, by performing a reprojection of Phat Elvis pericenters using the z = 0 positions and velocities of the subhaloes and a static MW-like potential. We conclude that pericenters calculated using this approach usually have good agreement with the true pericenter, albeit with a minor tendency to underestimate the pericenter and with occasional outliers.

8 CONCLUSIONS

In this work, we presented a comprehensive study of the internal dynamics of the brightest dSphs of the MW based on a flexible DF model. Going beyond the standard Jeans analysis often adopted

Downloaded from https://academic.oup.com/mnras/article/532/4/4157/7718108 by UC - Irvine user on 24 July 2025

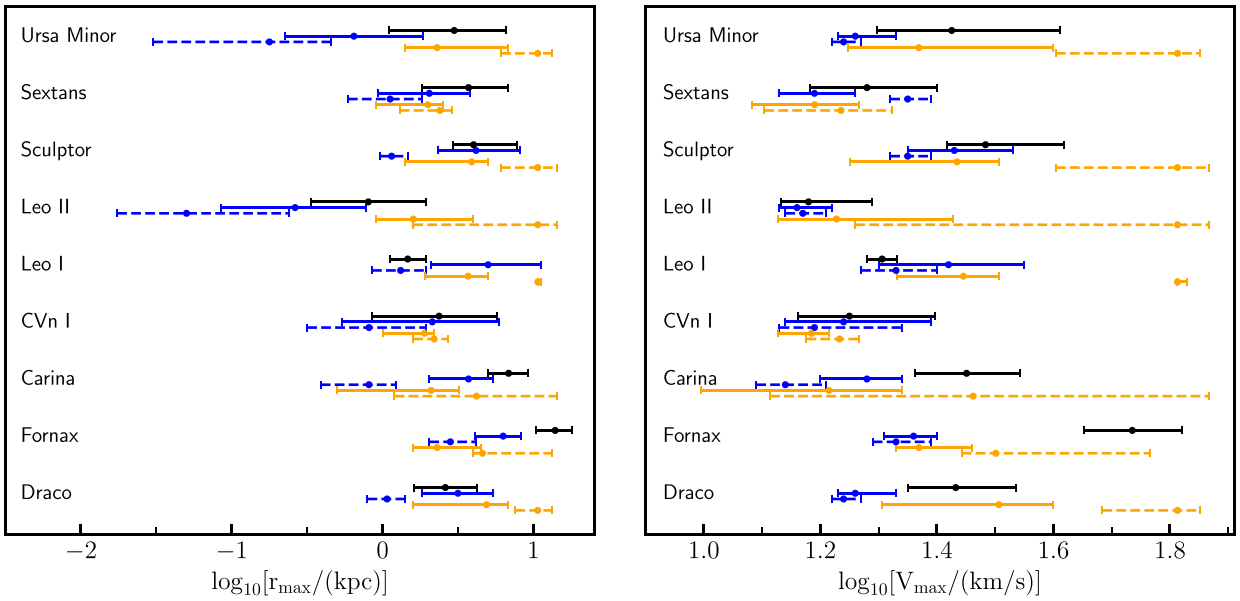

Figure 12. Inferences for r_{max} and V_{max} for the observed sample from this work, shown in black, compared to the Jeans analysis results of Kaplinghat et al. (2019), shown in blue, with their NFW case shown as blue solid lines and their cored isothermal case as blue dashed lines. We also compare to the analysis of Errani et al. (2018), in orange, with their cuspy case as orange solid lines and their cored case as orange dashed lines.

Table 4. Comparison of findings for DM density at 150 pc (ρ_{150}), in units of $10^7 M_\odot$ kpc^{-3}. The median posterior value and the 68 per cent confidence intervals are indicated. The references for comparison are (A) Read et al. (2019b), (B) Kaplinghat et al. (2019), isothermal case, (C) Kaplinghat et al. (2019), NFW case, and (D) Hayashi et al. (2020). Note that CVn I was not studied in references (A) or (D).

Name	This work	Ref A	Ref B	Ref C	Ref D
Draco	$18.8^{+3.7}_{-2.7}$	$23.6^{+2.0}_{-2.9}$	$21.2^{+5.4}_{-4.6}$	$21.7^{+2.5}_{-2.2}$	$23.5^{+12.8}_{-6.3}$
Fornax	$4.8^{+0.9}_{-0.5}$	$7.9^{+2.7}_{-1.9}$	$3.4^{+1.7}_{-1.3}$	$7.5^{+2.0}_{-1.4}$	$12.2^{+3.2}_{-2.3}$
Carina	$4.7^{+0.9}_{-0.7}$	$11.6^{+2.0}_{-2.2}$	$5.7^{+3.2}_{-1.7}$	$10.2^{+1.1}_{-0.9}$	$10.9^{+8.2}_{-3.2}$
CVn I	$10.5^{+5.4}_{-3.7}$	–	$13.5^{+5.3}_{-6.6}$	$13.4^{+3.1}_{-2.4}$	–
Leo I	$20.7^{+2.9}_{-2.9}$	$17.7^{+3.3}_{-3.4}$	$14.1^{+5.5}_{-4.5}$	$15.0^{+3.3}_{-2.4}$	$26.4^{+23.3}_{-9.1}$
Leo II	$17.1^{+2.1}_{-2.0}$	$18.4^{+1.7}_{-1.6}$	$13.4^{+4.3}_{-1.6}$	$17.0^{+2.3}_{-3.7}$	$20.2^{+12.7}_{-6.1}$
Sculptor	$14.7^{+1.8}_{-2.0}$	$14.9^{+2.8}_{-2.3}$	$16.1^{+2.9}_{-3.3}$	$17.1^{+2.1}_{-2.1}$	$21.4^{+12.6}_{-6.3}$
Sextans	$6.8^{+2.8}_{-1.9}$	$12.8^{+3.4}_{-2.9}$	$8.6^{+5.1}_{-3.5}$	$10.9^{+2.9}_{-1.8}$	$5.2^{+3.6}_{-2.3}$
Ursa minor	$17.5^{+7.3}_{-5.2}$	$15.3^{+3.5}_{-3.2}$	$25.4^{+6.2}_{-5.6}$	$25.1^{+3.0}_{-4.3}$	$23.8^{+38.6}_{-7.2}$

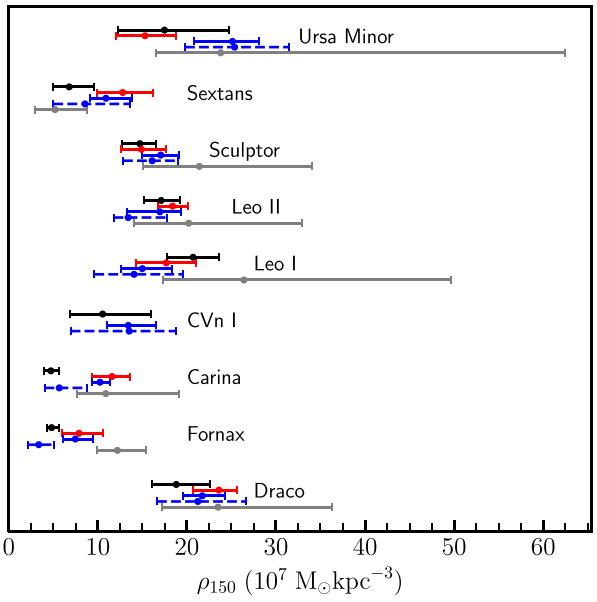

Figure 13. Inference of ρ_{150} from this work (black solid lines), compared to those of Read et al. (2019b) (red solid lines), the Jeans analysis of Kaplinghat et al. (2019) (NFW case: blue solid lines, cored isothermal case: blue dashed lines) and axisymmetric Jeans modelling of Hayashi et al. (2020) (grey solid lines).

for these systems, our method relies on a separable DF (Strigari et al. 2017) that describes the phase space of stellar tracers via 10 parameters, shaping the energy and angular momentum functional form. The DF approach we follow here is completed by the modelling of the gravitational potential of the system, for which we adopted a three-parameter cNFW distribution. This distribution is suitable for an investigation of both cuspy and cored DM haloes. For the first time in literature, we apply such a general approach to the set of 9 bright dSphs with well-measured kinematics, and perform a data-driven Bayesian analysis on the photometric and spectroscopic data available for these objects.

Our analysis via DF modelling is validated by the use of mock data extracted from the *Gaia* Challenge project. In particular, we adopted mock data sets to test the predictive capability of our approach both for cuspy and cored DM profiles, for cuspy and cored stellar profiles, for different level of embeddedness of the stellar distribution within the DM halo of the system and for spatially varying stellar orbital anisotropy profiles. From the study of the mock data we find that our DF approach is able to recover the true values of the V_{max} and r_{max} shape parameters of the underlying DM profile remarkably well, usually within the 68 per cent posterior probability region (see Fig. 2). It also has high accuracy for the recovery of key dynamical

Downloaded from https://academic.oup.com/mnras/article/532/4/4157/7718108 by UC - Irvine user on 24 July 2025

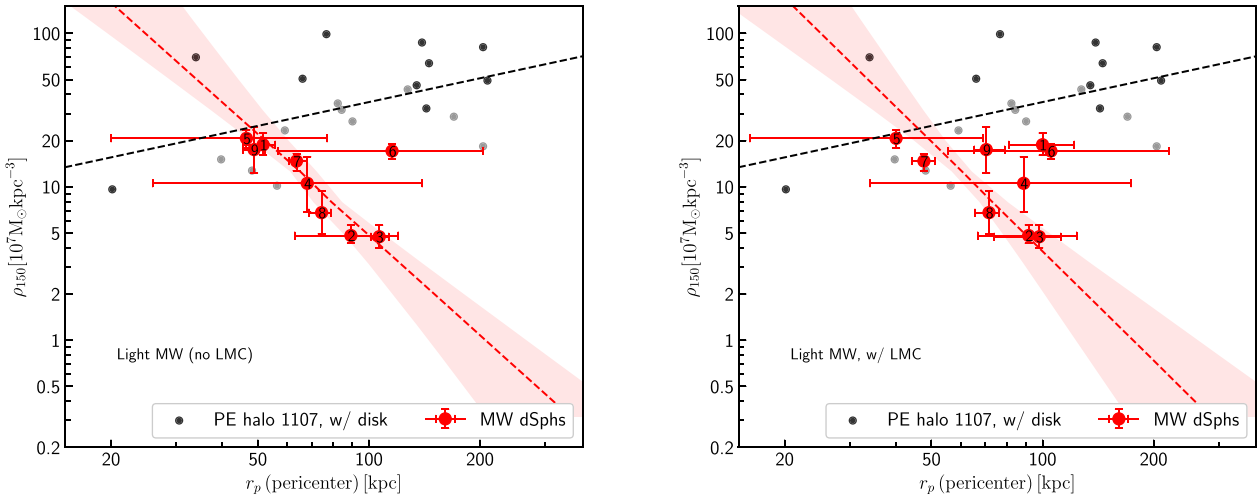

Figure 14. DM density at 150 pc (ρ_{150}) inferred from the DF fits for the bright MW dSphs versus orbital pericenter distance (r_p), in red, using the light MW model of Battaglia et al. (2022) and comparing to host halo 1107 of the Phat Elvis simulation (Kelley et al. 2019). The right panel uses the light MW model without the LMC, while the left panel uses the light MW model including the effect of the LMC. The error bars indicate the 68 per cent confidence interval. The best-fitting line through the observations is shown in dashed red, with the 68 per cent confidence interval in light red. The black circles indicate the 10 subhaloes with current radial positions greater than 50 kpc and with the largest V_{peak} for host halo 1107 of the Phat Elvis simulation. The grey circles denote the 10th through 20th largest V_{peak} subhaloes. The best-fitting regression line for the Phat Elvis points is shown as a black dashed line. The MW dSphs are numbered as follows: 1: Draco, 2: Fornax, 3: Carina, 4: CVn I, 5: Leo I, 6: Leo II, 7: Sculptor, 8: Sextans, 9: Ursa Minor.

quantities such as the total mass within the half-light radius, $M_{1/2}$ (see Fig. 4) and the inner local density of the system at 150 pc, ρ_{150} (Fig. 5). In contrast, the mock data show us that with this approach it remains difficult to reliably determine the size of the core of the DM inner halo or to obtain robust information about the orbital anisotropy profile of stellar tracers, both of which are difficulties also suffered by Jeans analysis. The accuracy of these predictions is higher for the cases where the stellar population is not too deeply embedded with the DM halo.

Equipped with these findings, our detailed study of the MW dSphs allowed us to revisit, reiterate and reinforce some well-known conclusions already drawn in literature within the standard Jeans analysis. Our study of the Classical dSphs via DF modelling provides a state-of-the-art inference of ρ_{150} in these objects. In particular, we find a low inner density for systems like Carina and Sextans, in contrast to galaxies like Draco and Leo II, characterized by inner densities approximately four times larger (Fig. 10). With the DF approach, we are then able to confirm the large diversity in the dark matter densities of these dark-matter dominated objects. These inferences of the inner density constitute key dynamical information that needs to be captured by any successful model of galaxy formation within the ΛCDM cosmological model, or another model where the dark matter is not made up of cold and collisionless DM particles.

We have reexamined the anticorrelation between dwarf spheroidal pericenters and density at 150 pc found in Kaplinghat et al. (2019), using our method rather than Jeans analysis and using more recent assessments of the pericenter determination by Battaglia et al. (2022). We also observe a negative correlation. This is inconsistent with both the dark-matter-only and disc versions of the Phat Elvis *N*-body simulation of Kelley et al. (2019, see Fig. 14). This inconsistency remains a compelling clue for investigating dark matter microphysics.

We observe that for Fornax and Carina, the results of our analysis with the cNFW profile point to the presence of a large core in these systems (Fig. E1). Most of the other dSphs have smaller cores or show no evidence for cores. Some care should be taken in considering this inference given the limited ability in inferring the core sizes in the mock data sets. Overall, our results argue that the DM core sizes are smaller than the respective half-light radii, which could be a further clue.

The results of our work are promising in the regard that the DF modelling has a similar constraining power to that of the spherical Jean analysis and other methods, despite varying a larger set of parameters needed for a broad description of the tracer phase-space DF. Natural extensions of this work will involve DF models that allow for multiple populations with separate metallicity distributions and non-sphericity in the stellar profiles.

This could allow for more robust inferences of the sizes of constant density cores in MW dSphs, and provide significant new constraints on proposed solutions to the too-big-to-fail problem.

ACKNOWLEDGEMENTS

We thank Matthew Walker and Andrew Pace for providing velocity dispersion data. We gratefully acknowledge a grant of computer time from TACC allocation AST20027. MK acknowledges support from National Science Foundation grant PHY-2210283.

DATA AVAILABILITY

The data underlying this article will be shared on reasonable request to the corresponding author.

REFERENCES

Adhikari S. et al., 2022, preprint (arXiv:2207.10638)
Agnello A., Evans N. W., 2012, ApJ, 754, L39
Amorisco N. C., Evans N. W., 2012, MNRAS, 419, 184
Battaglia G., Nipoti C., 2022, Nat. Astron., 6, 659
Battaglia G., Helmi A., Tolstoy E., Irwin M., Hill V., Jablonka P., 2008, ApJ, 681, L13

Downloaded from https://academic.oup.com/mnras/article/532/4/4157/7718108 by UC - Irvine user on 24 July 2025

Battaglia G., Helmi A., Breddels M., 2013, New Astron. Rev., 57, 52
Battaglia G., Taibi S., Thomas G. F., Fritz T. K., 2022, A&A, 657, A54
Benítez-Llambay A., Frenk C. S., Ludlow A. D., Navarro J. F., 2019, MNRAS, 488, 2387
Binney J., Mamon G. A., 1982, MNRAS, 200, 361
Binney J., Tremaine S., 2008, Galactic Dynamics. Princeton Univ. Press, Princeton
Bovy J., 2015, ApJS, 216, 29
Boylan-Kolchin M., Bullock J. S., Kaplinghat M., 2011, MNRAS, 415, 40
Breddels M. A., Helmi A., 2013, A&A, 558, A35
Breddels M. A., Helmi A., Van Den Bosch R. C., Van De Ven G., Battaglia G., 2012, in Reylé C., Robin A., Schultheis M., eds, Assembling the Puzzle of the Milky Way, Vol. 19, EPJ Web of Conferences, p. 03009
Breddels M. A., Helmi A., van den Bosch R. C., van de Ven G., Battaglia G., 2013, MNRAS, 433, 3173
Brown A. G. et al., 2018, A&A, 616, A1
Buckley M. R., Peter A. H. G., 2018, Phys. Rept., 761, 1
Bullock J. S., Boylan-Kolchin M., 2017, ARA&A, 55, 343
Cardona-Barrero S., Battaglia G., Nipoti C., Di Cintio A., 2023, MNRAS, 522, 3058
Chang L. J., Necib L., 2021, MNRAS, 507, 4715
Correa C. A., 2021, MNRAS, 503, 920
D'Souza R., Bell E. F., 2022, MNRAS, 512, 739
Despali G., Walls L. G., Vegetti S., Sparre M., Vogelsberger M., Zavala J., 2022, MNRAS, 516, 4543
Di Cintio A., Brook C. B., Macciò A. V., Stinson G. S., Knebe A., Dutton A. A., Wadsley J., 2014, MNRAS, 437, 415
Diakogiannis F. I., Lewis G. F., Ibata R. A., 2014, MNRAS, 443, 598
Diakogiannis F. I., Lewis G. F., Ibata R. A., Guglielmo M., Kafle P. R., Wilkinson M. I., Power C., 2017, MNRAS, 470, 2034
Diemand J., Kuhlen M., Madau P., 2007, ApJ, 667, 859
Elbert O. D., Bullock J. S., Garrison-Kimmel S., Rocha M., Oñorbe J., Peter A. H. G., 2015, MNRAS, 453, 29
Errani R., Peñarrubia J., Walker M. G., 2018, MNRAS, 481, 5073
Evans N. W., An J., Walker M. G., 2009, MNRAS, 393, L50
Ferrer F., Hunter D. R., 2013, JCAP, 09, 005
Foreman-Mackey D. et al., 2019, J. Open Source Softw., 4, 1864
Fritz T. K., Battaglia G., Pawlowski M. S., Kallivayalil N., Van Der Marel R., Sohn S. T., Brook C., Besla G., 2018, A&A, 619, 103
Governato F. et al., 2010, Nature, 463, 203
Guerra J., Geha M., Strigari L. E., 2023, ApJ, 943, 121
Hagen J. H., Helmi A., Breddels M. A., 2019, A&A, 632, A99
Hayashi K., Chiba M., 2012, ApJ, 755, 145
Hayashi E., Navarro J. F., Taylor J. E., Stadel J., Quinn T., 2003, ApJ, 584, 541
Hayashi K., Chiba M., Ishiyama T., 2020, ApJ, 904, 45
Hernquist L., 1990, ApJ, 356, 359
Jardel J. R., Gebhardt K., 2012, ApJ, 746, 89
Jardel J. R., Gebhardt K., Fabricius M. H., Drory N., Williams M. J., 2013, ApJ, 763, 91
Jeans J. H., 1915, MNRAS, 76, 70
Jiang F., Kaplinghat M., Lisanti M., Slone O., 2021, preprint (arXiv:2108.03243)
Kaplinghat M., Valli M., Yu H. B., 2019, MNRAS, 490, 231
Kelley T., Bullock J. S., Garrison-Kimmel S., Boylan-Kolchin M., Pawlowski M. S., Graus A. S., 2019, MNRAS, 487, 4409
Kim S. Y., Peter A. H. G., 2021, preprint (arXiv:2106.09050)
Kowalczyk K., Lokas E. L., 2022, A&A, 659, A119
Kowalczyk K., Łokas E. L., Valluri M., 2017, MNRAS, 470, 3959
Kowalczyk K., Łokas E. L., Valluri M., 2018, MNRAS, 476, 2918
Kowalczyk K., Del Pino A., Łokas E. L., Valluri M., 2019, MNRAS, 482, 5241
Lacroix T., Stref M., Lavalle J., 2018, JCAP, 09, 040
Lepage P. G., 1978, J. Comput. Phys., 27, 192
Lewis A., 2019, preprint (arXiv:1910.13970)
Li H., Widrow L. M., 2021, MNRAS, 503, 1586
Li Z.-Z., Qian Y.-Z., Han J., Li T. S., Wang W., Jing Y. P., 2020, ApJ, 894, 10
Łokas E. L., 2009, MNRAS, 394, L102
Łokas E. L., Mamon G. A., 2003, MNRAS, 343, 401
Lokas E. L., Mamon G. A., Prada F., 2005, MNRAS, 363, 918
Mateo M., Olszewski E. W., Walker M. G., 2008, ApJ, 675, 201
McConnachie A. W., 2012, AJ, 144, 4
Merrifield M. R., Kent S. M., 1990, AJ, 99, 1548
Muñoz R. R., Côté P., Santana F. A., Geha M., Simon J. D., Oyarzún G. A., Stetson P. B., Djorgovski S. G., 2018, ApJ, 860, 66
Nadler E. O., Gluscevic V., Boddy K. K., Wechsler R. H., 2019, ApJ, 878, L32
Nadler E. O. et al., 2021a, Phys. Rev. Lett., 126, 091101
Nadler E. O., Birrer S., Gilman D., Wechsler R. H., Du X., Benson A., Nierenberg A. M., Treu T., 2021b, ApJ, 917, 7
Navarro J. F., Frenk C. S., White S. D. M., 1996, ApJ, 462, 563
Nishikawa H., Boddy K. K., Kaplinghat M., 2020, Phys. Rev. D, 101, 063009
Pace A. B. et al., 2020, MNRAS, 495, 3022
Pace A. B., Erkal D., Li T. S., 2022, ApJ, 940, 136
Pascale R., Posti L., Nipoti C., Binney J., 2018, MNRAS, 480, 927
Patel E. et al., 2020, ApJ, 893, 121
Penarrubia J., Navarro J. F., McConnachie A. W., 2008, ApJ, 673, 226
Peñarrubia J., Pontzen A., Walker M. G., Koposov S. E., 2012, ApJ, 759, L42
Petac M., Ullio P., Valli M., 2018, JCAP, 12, 039
Plummer H. C., 1911, MNRAS, 71, 460
Read J. I., Walker M. G., Steger P., 2018, MNRAS, 481, 860
Read J., Gieles M., Kawata D., 2019a, The Gaia Challenge. Available at: http://astrowiki.ph.surrey.ac.uk/dokuwiki/doku.php
Read J. I., Walker M. G., Steger P., 2019b, MNRAS, 484, 1401
Read J. I. et al., 2021, MNRAS, 501, 978
Richardson T., Fairbairn M., 2014, MNRAS, 441, 1584
Rocha M., Peter A. H., Bullock J. S., Kaplinghat M., Garrison-kimmel S., Oñorbe J., Moustakas L. A., 2013, MNRAS, 430, 81
Sales L. V., Wetzel A., Fattahi A., 2022, Nature Astron., 6, 897
Salucci P., Burkert A., 2000, ApJ, 537, L9
Sameie O., Yu H.-B., Sales L. V., Vogelsberger M., Zavala J., 2020, Phys. Rev. Lett., 124, 141102
Sawala T. et al., 2016, MNRAS, 457, 1931
Schwarzchild M., 1980, ApJS, 43, 435
Shah N., Adhikari S., 2024, MNRAS, 529, 4611
Simon J. D., 2019, ARA&A, 57, 375
Slone O., Jiang F., Lisanti M., Kaplinghat M., 2021, preprint (arXiv:2108.03243)
Spencer M. E., Mateo M., Walker M. G., Olszewski E. W., 2017, ApJ, 836, 202
Strigari L. E., 2018, Rep. Prog. Phys., 81, 056901
Strigari L. E., Koushiappas S. M., Bullock J. S., Kaplinghat M., 2007, Phys. Rev. D (Particles, Fields, Gravitation and Cosmology), 75, 83526
Strigari L. E., Bullock J. S., Kaplinghat M., Simon J. D., Geha M., Willman B., Walker M. G., 2008, Nature, 454, 1096
Strigari L. E., Frenk C. S., White S. D., 2010, MNRAS, 408, 2364
Strigari L. E., Frenk C. S., White S. D. M., 2017, ApJ, 838, 123
Valli M., Yu H.-B., 2018, Nat. Astron., 2, 907
Van Den Bosch R. C., Van De Ven G., Verolme E. K., Cappellari M., De Zeeuw P. T., 2008, MNRAS, 385, 647
Vogelsberger M., Zavala J., Loeb A., 2012, MNRAS, 423, 3740
Vogelsberger M., Zavala J., Simpson C., Jenkins A., 2014, MNRAS, 444, 3684
Walker M. G., Penarrubia J., 2011, ApJ, 742, 20
Walker M. G., Mateo M., Olszewski E. W., Bernstein R., Wang X., Woodroofe M., 2006, AJ, 131, 2114
Walker M. G., Mateo M., Olszewski E. W., Narrubia J. P., Evans N. W., Gilmore G., 2009, ApJ, 704, 1274
Walker M. G., Olszewski E. W., Mateo M., 2015, MNRAS, 448, 2717
Weinberg D. H., Bullock J. S., Governato F., De Naray R. K., Peter A. H., 2015, Proc. Natl. Acad. Sci. USA, 112, 12249
Wheeler C. et al., 2017, MNRAS, 465, 2420

Downloaded from https://academic.oup.com/mnras/article/532/4/4157/7718108 by UC - Irvine user on 24 July 2025

Wolf J., Martinez G. D., Bullock J. S., Kaplinghat M., Geha M., Muñoz R. R., Simon J. D., Avedo F. F., 2010, MNRAS, 406, no
Wu X., Tremaine S., 2006, ApJ, 643, 210
Yang D., Nadler E. O., Yu H.-B., 2023, ApJ, 949, 67
Zeng Z. C. et al., 2023, preprint (arXiv:2310.09910)
Zhao H., 1996, MNRAS, 278, 488
Zhu L., Van De Ven G., Watkins L. L., Posti L., 2016, MNRAS, 463, 1117

APPENDIX A: COMPARISON TO STRIGARI ET AL. (2017) FOR SCULPTOR

Because our approach is similar to that of Strigari et al. (2017), we created a modified version of our model that maximizes its comparability to the one in that work, and compare the results of the two models here. To maximize comparability, we make the following changes to our model: (a) remove the factor of $\frac{1}{2}$ from equation (13), (b) remove the normalization term $n_{\rm f}$ in equation (14) and allow the parameter w to vary freely in the MCMC analysis, (c) set $b_{\rm in} = 0$, (d) set $\alpha = 1$, (e) set $c = 0$, which forces the DM profile to be an NFW profile, and (f) remove the VSP chi square component. We then run our model on the same Sculptor metal poor and metal-rich population data as was used in Strigari et al. (2017), i.e. the surface density and dispersion data from Battaglia et al. (2008). The results are shown in Fig. A1. The top panel shows the results for the metal poor case, the bottom panel shows the metal-rich case. Our results are shown in black and the results from fig. 4 of Strigari et al. (2017) are shown in blue (metal poor) and red (metal rich), respectively. Their result correspond fairly closely with ours.

APPENDIX B: VIRIAL SHAPE PARAMETER

The virial shape parameter is derived from the fourth-order projected virial theorem (Merrifield & Kent 1990), and for approximately spherical systems it can take two forms (Richardson & Fairbairn 2014). Following Kaplinghat et al. (2019), we utilize the first form, which we label here the VSP:

$$\mathrm{VSP} = \frac{1}{2}\int_0^\infty \mathrm{d}R^2\,\Sigma\langle v_{\rm los}^4\rangle = \frac{G}{5}\int_0^\infty \mathrm{d}r^2 M(5-2\beta)\nu\sigma_{\rm r}^2, \qquad \text{(B1)}$$

where M denotes the mass DF, β is the anisotropy parameter, ν is the stellar density and $\langle v_{\rm los}^4\rangle$ is the fourth moment of the line-of-sight velocity distribution. To calculate the VSP from the DF, we integrate

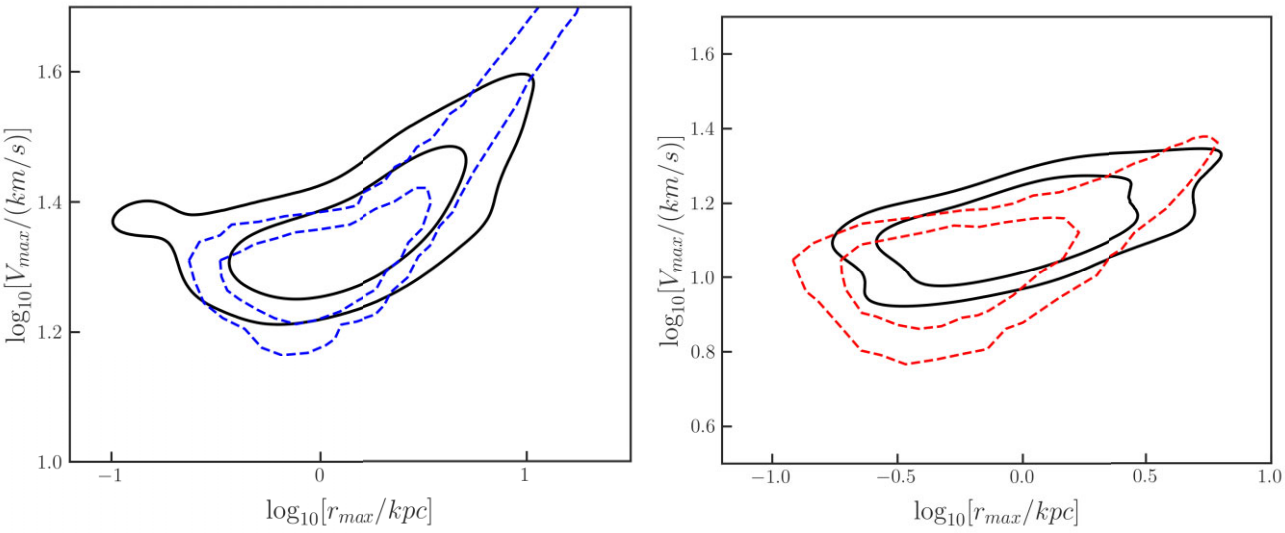

Figure A1. Comparison of the results of the modified model (shown in black) for $r_{\rm max}$ versus $V_{\rm max}$ to the NFW results of Strigari et al. (2017) for Sculptor. The lines indicate the 68 per cent and 90 per cent confidence levels. *Top panel:* Metal-poor stellar population. The results from Strigari et al. (2017) are in blue. *Bottom Panel:* Metal-rich stellar population. The results from Strigari et al. (2017) are in red. Note that for this figure only we follow the convention from Strigari et al. (2017) that the outer contour lines represent the 90 per cent confidence level rather than 95 per cent.

Downloaded from https://academic.oup.com/mnras/article/532/4/4157/7718108 by UC - Irvine user on 24 July 2025

the fourth velocity moment as follows:

$$(2\pi)\mathrm{vsp} = \int \mathrm{d}^3 r \mathrm{d}^3 v \; v_z^4 f(E, L) \; .$$

Note that there is no factor of N_* because the DF is normalized to unity over the entire phase space. Now write

$$v_r = v\cos\eta, \; v_\theta = v\sin\eta\cos\psi.$$

Then,

$$v_z = \hat{z} \times \vec{v} = v_r\cos\theta - v_\theta\sin\theta = v(\cos\theta\cos\eta - \sin\theta\sin\eta\cos\psi)$$

and

$$\mathrm{VSP} = \int r^2 \mathrm{d}r \; \mathrm{dcos}\theta \; v^2 \mathrm{d}v \; \mathrm{d}\psi \mathrm{dcos}\eta \; v_z^4 f(E, L).$$

Since $E = \Psi - v^2/2$ and $L = r v_\mathrm{t} = r v \sin\eta$, we can first do the θ and ψ integrals over v_z^4. It can be shown that

$$\int_0^{2\pi} \mathrm{d}\psi \int_{-1}^{1} \mathrm{dcos}\theta (\cos\theta\cos\eta - \sin\theta\sin\eta\cos\psi)^4 = 4\pi/5$$

hence,

$$\mathrm{VSP} = (4\pi/5)\int_0^{r_\mathrm{t}} r^2 \mathrm{d}r \int_0^{\sqrt{2\Psi(r)}} v^6 \mathrm{d}v \int_{-1}^{1} \mathrm{dcos}\eta \; f(E, L) \; . \quad \text{(B2)}$$

For data sets with measured line-of-sight velocities, the VSP can be calculated as follows. In our coordinate system, the z-axis is the line of sight. First, the mean value of v_z is subtracted from each $v_{z,i}$ to remove bulk motion of the galaxy. The VSP is then

$$\mathrm{VSP} = \frac{1}{2\pi N_*} \sum_{i=1}^{N_*} v_{z,i}^4 \; . \quad \text{(B3)}$$

For the mock data sets, we wish to find the an estimate of the distribution of the VSP given the one set of sampled velocities. We do so by generating 10 000 ensembles of binned velocity data, each with length N_*, from a Pearson distribution of Type VII, with the same star count and velocity dispersion in each bin as the original data set. To simulate measurement uncertainty, we add Gaussian error with a standard deviation of 2 km s^{-1}. The kurtosis of the Pearson distribution is adjustable via a parameter, and that parameter is iteratively varied until the kurtosis of the entire ensemble matches that of the original data set. We then tabulate the 15.9, 50, and 84.1 percentile values of the VSP of the entire ensemble, which are used as estimators for the mean and standard deviation of the VSP. Those values are used as data for the DF model and are tabulated for the mock data sets in Table O1.

APPENDIX C: FULL LIKELIHOOD FUNCTION

Consider a population of w stars in a potential Φ and with a DF f. Our goal is to estimate Φ and f based on the star population. For star i, we have position coordinates $R_\mathrm{i} = \sqrt{x_\mathrm{i}^2 + y_\mathrm{i}^2}$, and we have velocity coordinate $v_{z,\mathrm{i}}$ (but we do not generally know z_i, $v_{x,\mathrm{i}}$ or $v_{y,\mathrm{i}}$). The best estimate of Φ and f is the one that maximizes the likelihood function

$$\mathrm{LH}(\Phi, f|[R_\mathrm{i}, v_{z,\mathrm{i}}]). \quad \text{(C1)}$$

By Bayes Theorem, we instead estimate the posterior and prior probabilities

$$\mathrm{LH}(\Phi, f|[R_\mathrm{i}, v_{z,\mathrm{i}}]) = \mathrm{LH}([R_\mathrm{i}, v_{z,\mathrm{i}}]|\Phi, f)\frac{P(\Phi, f)}{P([R_\mathrm{i}, v_{z,\mathrm{i}}])} \; , \quad \text{(C2)}$$

where $\mathrm{LH}([R_\mathrm{i}, v_{z,\mathrm{i}}]|\Phi, f)$ is the posterior probability of observing the given data with a particular Φ and f, and $P(\Phi, f)$ is the prior probability for observing Φ and f, and incorporates any prior beliefs. The probability of observing the data for our model, $P([R_\mathrm{i}, v_{z,\mathrm{i}}])$, also known as the 'evidence', is not generally known, but as it is a constant factor it will not affect our attempts to maximize the likelihood function.

We wish to employ the DF as a probability of finding a star i at radius R and line-of-sight velocity v_z. The probability can be written as

$$p_{*,\mathrm{i}}(R_\mathrm{i}, v_{z,\mathrm{i}}) = 2\pi \int_{-\infty}^{\infty} v_R dv_R \int_{-\infty}^{\infty} \mathrm{d}z \; f(E_\mathrm{i}, L_\mathrm{i}) \; . \quad \text{(C3)}$$

The composite likelihood for all stars in the data set is then

$$\mathrm{LH}([R, v_z]|\Phi, f) = \prod_{i=1}^{w} p_{*,\mathrm{i}}(R_\mathrm{i}, v_{z,\mathrm{i}}) \; , \quad \text{(C4)}$$

and the log likelihood is then

$$\mathrm{LLH} \triangleq \log(\mathrm{LH}([R, v_z]|\Phi, f))) = \sum_{i=1}^{w} \log(p_{*,\mathrm{i}}(R_\mathrm{i}, v_{z,\mathrm{i}})) \; . \quad \text{(C5)}$$

Computationally, we have a vector of parameters $\boldsymbol{p} = \{r_\mathrm{s}, v_\mathrm{s}, \Phi_\mathrm{lim}, e, a, q, E_\mathrm{c}, d, L_\beta, b_\mathrm{in}, b_\mathrm{out}, w\}$ for which we want to calculate a given likelihood. The normalization factor n_f may be factored out of the sum, and LLH becomes

$$\mathrm{LLH}(\boldsymbol{p}) = n_\mathrm{f}(\boldsymbol{p}) \sum_{i=1}^{w} \log\Big(\int_{-\infty}^{\infty} \mathrm{d}v_R \int_{-\infty}^{\infty} \mathrm{d}z \; h\big(\boldsymbol{p}, E(\boldsymbol{x_\mathrm{i}}, \boldsymbol{v_\mathrm{i}})\big) g\big(\boldsymbol{p}, L(\boldsymbol{x_\mathrm{i}}, \boldsymbol{v_\mathrm{i}})\big)\Big) \; , \quad \text{(C6)}$$

where the functions h and g are given in equations (12) and (13).

APPENDIX D: BINNING OF VELOCITY DISPERSION DATA

Here, we describe our procedure for binning the velocity dispersion data. For the observed sample, the data consists of the right ascension and declination coordinates for each star, the LOS velocity for each star, and the uncertainty of the LOS velocity measurement. The position data is converted to physical δx and δy coordinates using the adopted distance to the galaxy specified in Table 2. The centroid is calculated as the coordinates that minimize the sum of the squared distances from each star to the center. These correspond closely to the galaxy coordinates cited in the NASA/IPAC Extragalactic Database (https://ned.ipac.caltech.edu). To account for the ellipticity of the galaxies, we draw elliptical bins based on the position angle and ellipticity noted in Table 2. We use Sturges' Rule to determine the number of bins, i.e. $B = \log_2(N_\mathrm{stars}) + 1$. The bin boundaries are chosen so that there are an equal number of stars in each bin to the maximum extent possible. For the Gaia Challenge data, the same process is used, but is simplified because the data center coordinates are known, and the data were generated with spherical symmetry so no adjustment for ellipticity is required.

Our method for estimating the binned velocity dispersions closely follows the maximum likelihood approach described in Walker et al. (2006). We let v_ij, u_ij and σ_ij be the measured LOS velocity, the true LOS velocity and the measurement uncertainty, for star i of N_j stars in bin j of B bins. Then $v_\mathrm{ij} = u_\mathrm{ij} + \sigma_\mathrm{ij}\epsilon_\mathrm{ij}$, and the ϵ_ij have a standard Gaussian distribution. The variability in v_ij comes from two sources: the intrinsic LOS velocity dispersion in the u_ij, which we denote σ_j, and the measurement uncertainties σ_ij. We assume that the v_ij have a Gaussian distribution with mean equal to the mean

Downloaded from https://academic.oup.com/mnras/article/532/4/4157/7718108 by UC - Irvine user on 24 July 2025

true velocity $\langle u \rangle$. The joint probability over all of the observations is therefore:

$$\mathrm{LH} = \prod_{j=1}^{B} \prod_{i=1}^{N_j} \frac{1}{\sqrt{2\pi\left(\sigma_{\mathrm{ij}}^2 + \sigma_{\mathrm{j}}^2\right)}} \exp\left(-\frac{(v_{\mathrm{ij}} - \langle u \rangle)^2}{2\left(\sigma_{\mathrm{ij}}^2 + \sigma_{\mathrm{j}}^2\right)}\right). \quad \text{(D1)}$$

We use MCMC analysis to determine posterior distributions for $\langle u \rangle$ and the σ_{j}. We use the EMCEE sampler (Foreman-Mackey et al. 2019). We explored using velocity dispersion directly as the parameter of interest, as well as using $\log_{10}$ of the velocity dispersions, and found that using the logarithm resulted in Gaussian distributions for the posterior distributions, while using the dispersions themselves did not. We therefore use $\langle u \rangle$ and $\log_{10}(\sigma_{\mathrm{j}})$ as parameters in the MCMC analysis. The resulting binned data values and their uncertainties are available in the online material.

APPENDIX E: CORE RADII INFERENCES FOR MOCK DATA AND OBSERVED DWARFS

The parameter $\log_{10}[r_{\mathrm{c}}/\mathrm{kpc}]$ is allowed to vary in the model to explore the best fitting value, with prior limits $-2 < \log_{10}[r_{\mathrm{c}}/\mathrm{kpc}] < 1$. As described in Section 2.1, the core radius r_{core} is calculated as the radius at which the density falls to one-half its central value. The true core radii of the mock data sets are either 0 kpc (NFW) or 0.26 kpc (cored), corresponding to $\log_{10}$ values of $-\infty$ and -0.585, respectively, although we use -2 as a practical lower limit, corresponding to $r_{\mathrm{core}} = 0.01$ kpc. The top panels of Fig. E1 shows a composite plot of the posteriors for the 16 NFW data sets in the left panel and the 16 cored data sets in the right panel. The model shows some ability to distinguish between the two profiles, with an uncertainty of approximately 0.5–1.0 dex, although there is bias towards lower values for the cored profiles. The NFW data sets uniformly prefer small cores. The cored data sets generally prefer large core solutions, except for some of the most deeply embedded data sets with $r_*/r_{\mathrm{s}} = 0.1$.

We also present the core radius posteriors of the observed sample here, for easier comparison to the mock data results. As shown in the bottom panels of Fig. E1, many of the observed sample prefer small cores, consistent with the NFW profile. However, Fornax and Carina prefer non-zero cores with large radii of approximately 0.5 and 0.3 kpc, respectively. We note that Peñarrubia et al. (2012) found cores in Fornax and Sculptor by exploiting separate chemo-dynamical subcomponents, although Strigari et al. (2017) found only a weak preference for a core in Sculptor and that both cored and NFW profiles were good fits. Hayashi et al. (2020) found that Carina, Sextans, Sculptor, and Fornax favour smaller (core-like) DM inner slopes, using axisymmetric Jeans analysis. Other authors finding a likely core in Fornax include Walker & Penarrubia (2011), Jardel & Gebhardt (2012), and Pascale et al. (2018). A key difference between our work and previous work is the use of mock data to validate our inferences.

On the other hand, Draco, Sculptor, and Sextans show evidence for a small core of about 100 pc. The left panel of Fig. E1 demonstrates that if the true profile is an NFW profile, the model posterior is unlikely to resemble those of Draco, Fornax, Carina, Sculptor, and Sextans. Draco has been thought to be cuspy in prior works (Read et al. 2018, 2019b; Hayashi et al. 2020); our finding is for a small core but with a high density, so in that regard all studies seem to agree with each other.

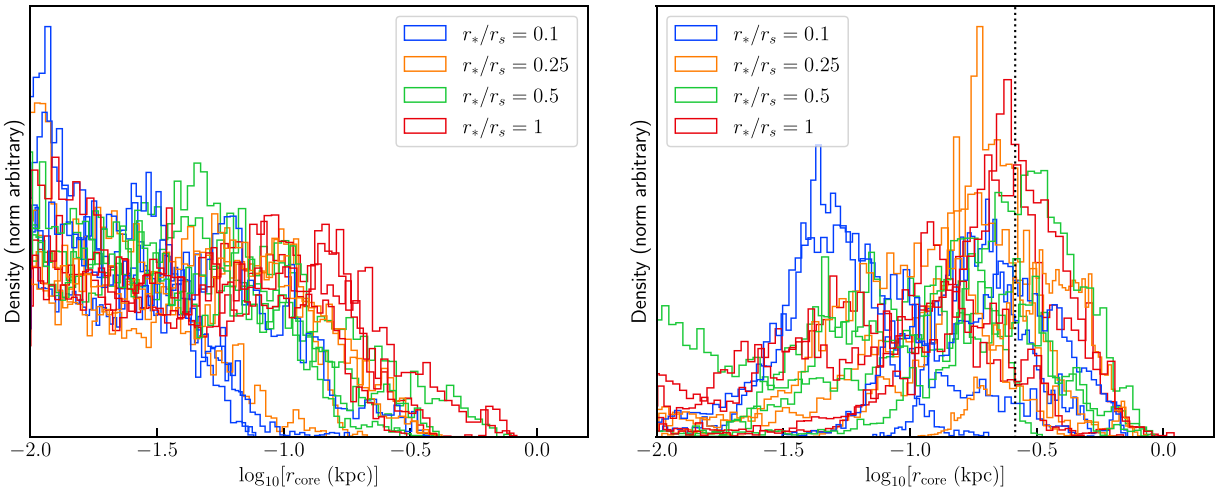

Figure E1. Posterior histograms of $\log_{10}[r_{\mathrm{core}}/\mathrm{kpc}]$, with mock data sets. *Left:* The 16 mock data sets with NFW DM profiles. The true value of $\log_{10}[r_{\mathrm{core}}/\mathrm{kpc}]$ is $-\infty$ (corresponding to $r_{\mathrm{core}} = 0$ kpc), although we limit the parameter to -2 in $\log_{10}$ space (corresponding to $r_{\mathrm{core}} = 0.01$ kpc). *Right:* The 16 mock data sets with cored DM profiles. The true value is -0.585 (corresponding to $r_{\mathrm{core}} = 0.26$ kpc) and is indicated by the black dotted line.

Downloaded from https://academic.oup.com/mnras/article/532/4/4157/7718108 by UC - Irvine user on 24 July 2025

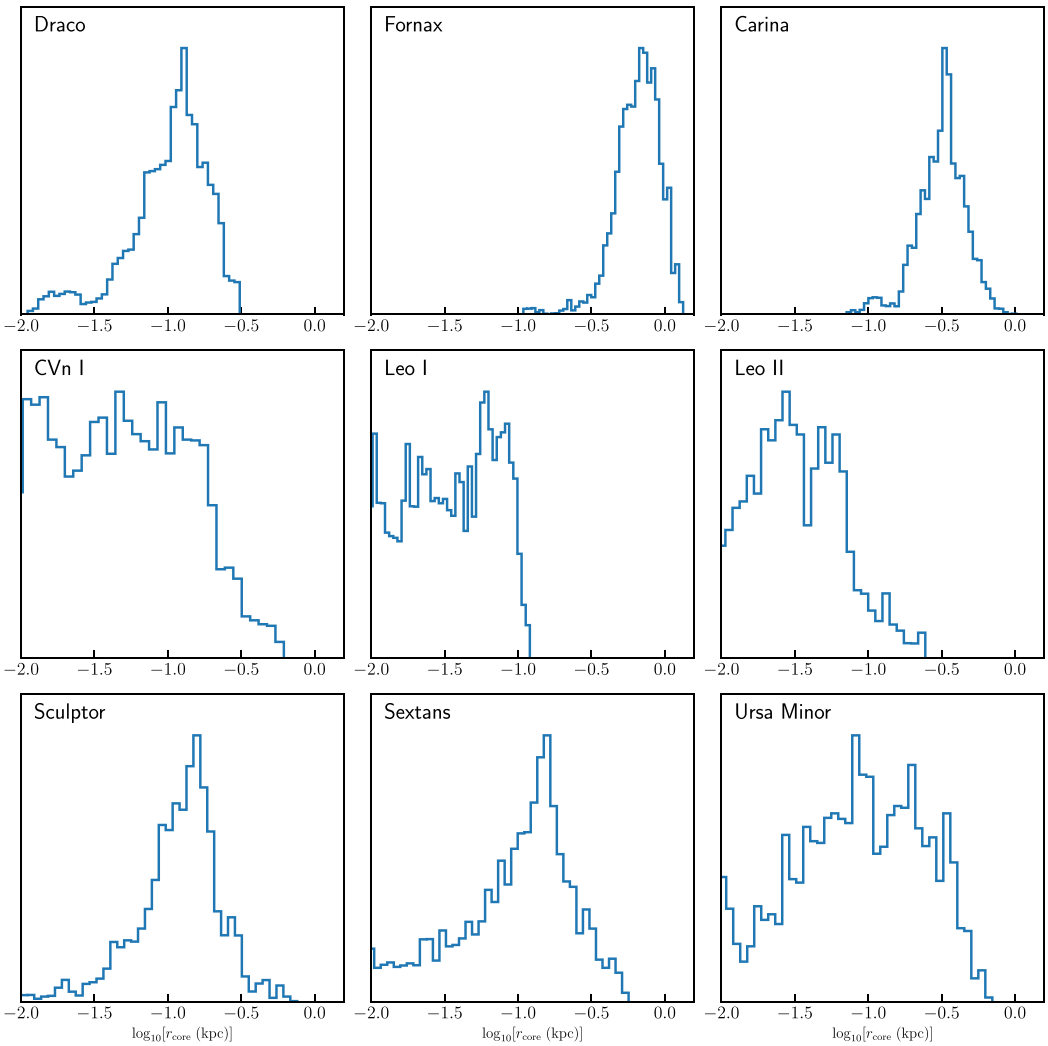

Figure E2. Posterior histograms of $\log_{10}[r_{\rm core}/{\rm kpc}]$, with observed dSphs in the three rows. *Left:* The 16 mock data sets with NFW DM profiles. The true value of $\log_{10}[r_{\rm core}/{\rm kpc}]$ is $-\infty$ (corresponding to $r_{\rm core} = 0$ kpc), although we limit the parameter to -2 in $\log_{10}$ space (corresponding to $r_{\rm core} = 0.01$ kpc). *Right:* The 16 mock data sets with cored DM profiles. The true value is -0.585 (corresponding to $r_{\rm core} = 0.26$ kpc) and is indicated by the black dotted line. *Bottom three rows:* Inferences of $\log_{10}[r_{\rm core}/{\rm kpc}]$ for the observed sample. The modes for Fornax and Carina are at approximately $\log_{10}[r_{\rm core}/{\rm kpc}]$ of -0.3 and -0.5, respectively, which correspond to $r_{\rm core}$ of 0.3 and 0.5 kpc. The other galaxies have modes at or less than ~ 0.1 kpc.

APPENDIX F: ANISOTROPY AT HALF-LIGHT RADIUS

Fig. F1 shows the true and predicted posteriors for the anisotropy parameter β at the half-light radius for the mock data sets. Half of the mock data sets are anisotropic over their entire range, while the other half have rising β profiles, with a true value between 0.4 and 0.6 at the half-light radius. For the isotropic data sets, the model predictions have median values centred near zero and with a range of -0.2 to 0.2. For the anisotropic data sets, the model tends to systematically underestimate β, except for least embedded data sets denoted in red.

Downloaded from https://academic.oup.com/mnras/article/532/4/4157/7718108 by UC - Irvine user on 24 July 2025

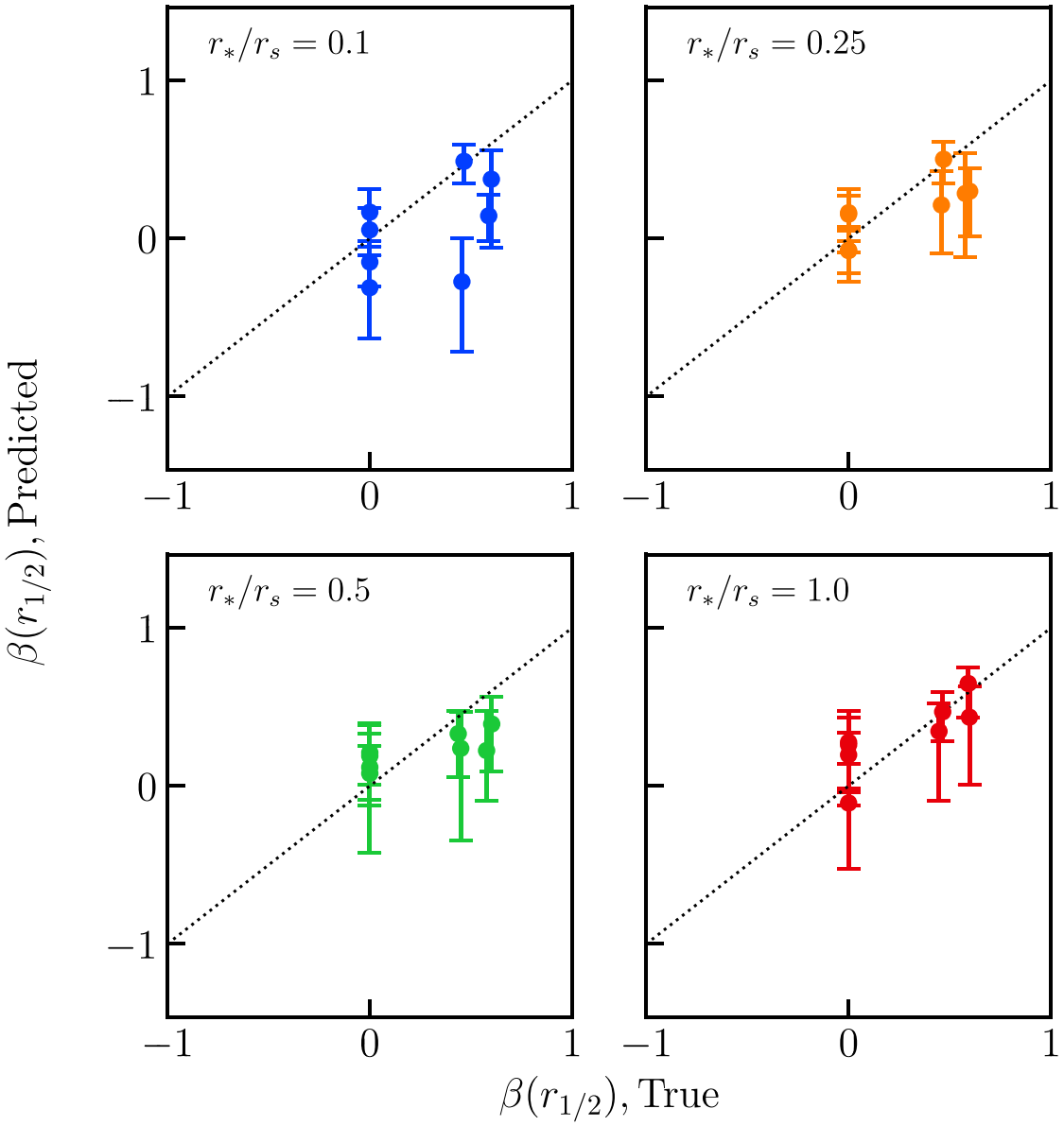

Figure F1. True and predicted values for $\beta(r_{1/2})$ for the 32 mock data sets, segregated by embeddedness. The diagonal line indicates equality between the true and predicted values.

APPENDIX G: CORE PARAMETER POSTERIORS OF THE OBSERVED SAMPLE

The posteriors for $c = r_c/r_s$ are shown in Fig. G1. Most of the sample shows a preference for nearly zero values of the core parameter, indicating a density profile that is close to the NFW profile. However, Fornax and Carina do have significant tails above $c = 1$. In that area of parameter space, the scale radius r_s is smaller than the core radius r_c, so that they can be said to switch roles in defining the shape of the profile (see equation 11).

Downloaded from https://academic.oup.com/mnras/article/532/4/4157/7718108 by UC - Irvine user on 24 July 2025

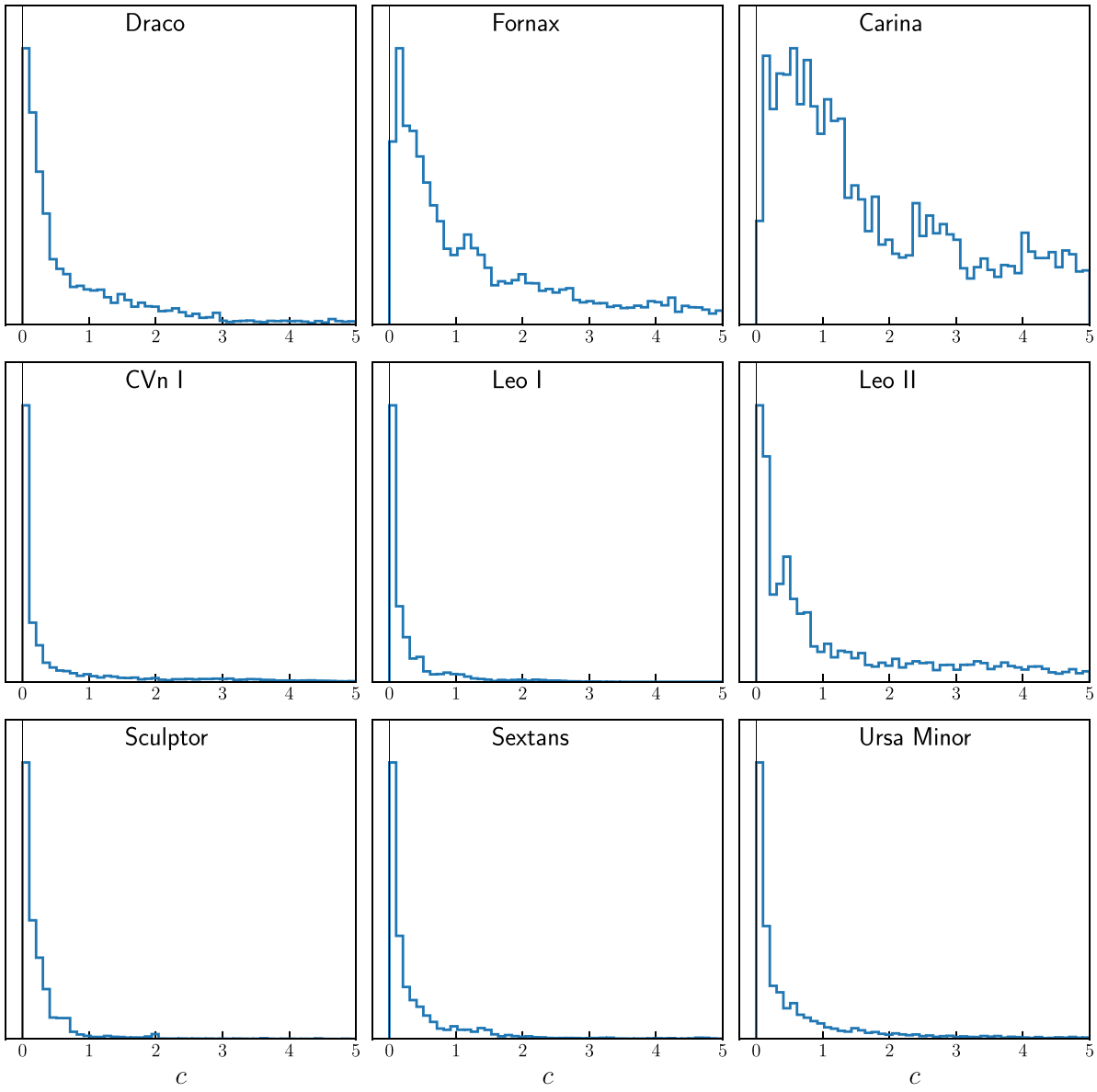

Figure G1. Posteriors of the core parameter, $c = r_c/r_s$ for the bright MW dSphs. Only Fornax and Carina show a significant posterior above $c = 1$.

APPENDIX H: VELOCITY DISPERSION ANISOTROPY IN THE OBSERVED SAMPLE

The posteriors for the anisotropy parameter $\beta(r_{1/2})$ for the observed sample are shown in Fig. H1. In the tests of the mock data in predicting this parameter, the inferences had limited accuracy and tended to understate the true value of β where the value was positive, although the accuracy was better where the star populations were the least embedded. Here, the inferences for Draco and Carina are for positive anisotropy, and as neither of the two are particularly deeply embedded (see Fig. I1), and given that a bias lower will cause their true anisotropy to be even higher, it seems likely that Draco and Carina are indeed likely to have positive anisotropy at their half-light radii.

Downloaded from https://academic.oup.com/mnras/article/532/4/4157/7718108 by UC - Irvine user on 24 July 2025

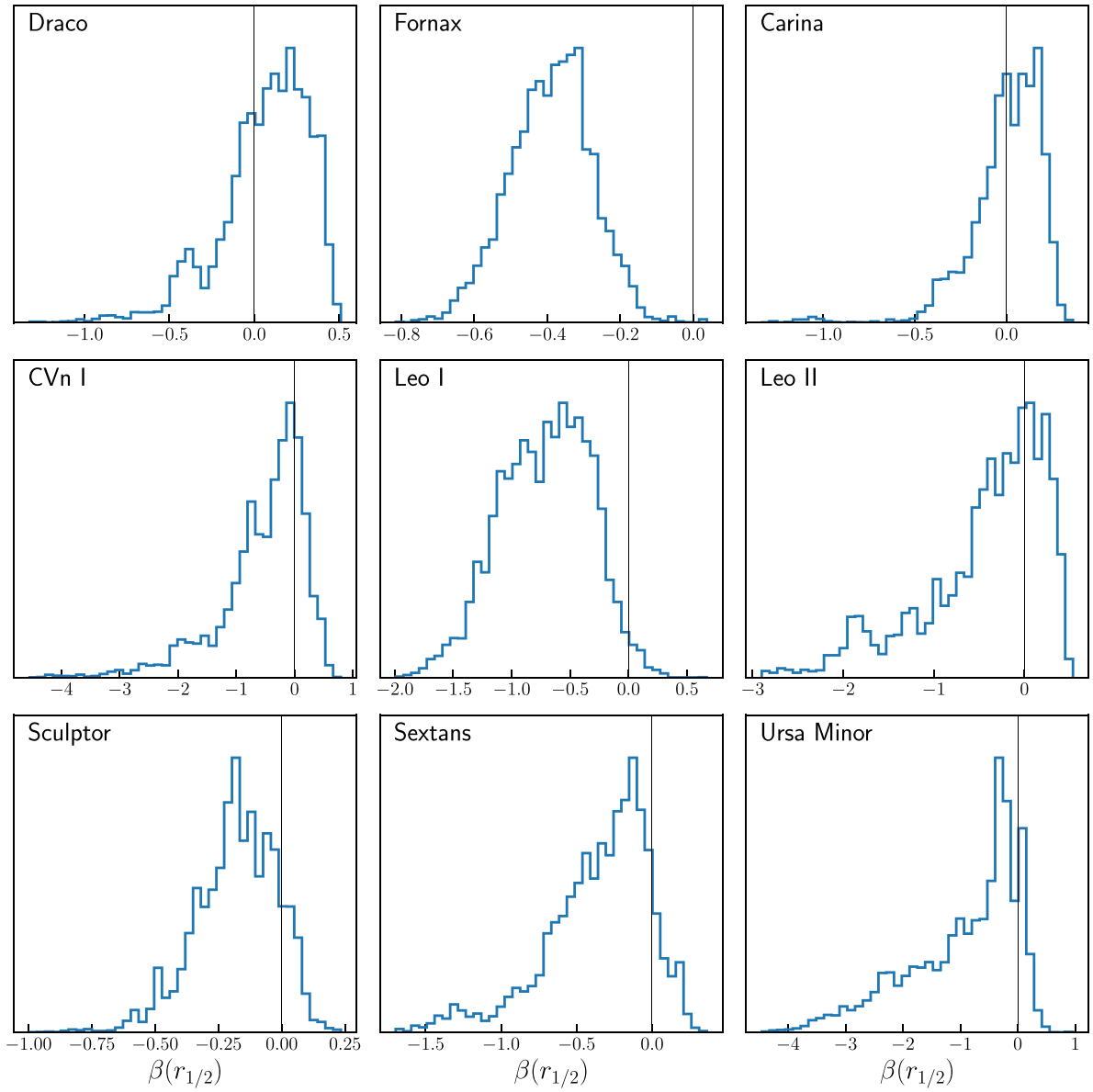

Figure H1. Posteriors of anisotropy parameter β at the half-light radius for the bright MW dSphs.

APPENDIX I: EMBEDDEDNESS OF THE OBSERVED SAMPLE

Because the degree to which the stellar population is embedded in the DM potential is an important factor for the accuracy of the model, we examine this in Fig. I1, which shows $r_{1/2}/r_s$ for the observed sample. Sculptor and Fornax have lowest inferences, with median values of 0.23 and 0.25, respectively. Though still less embedded than the most embedded mock data sets, the inferences for Sculptor and Fornax could be vulnerable to the types of biases seen in the most embedded mock data sets.

Downloaded from https://academic.oup.com/mnras/article/532/4/4157/7718108 by UC - Irvine user on 24 July 2025

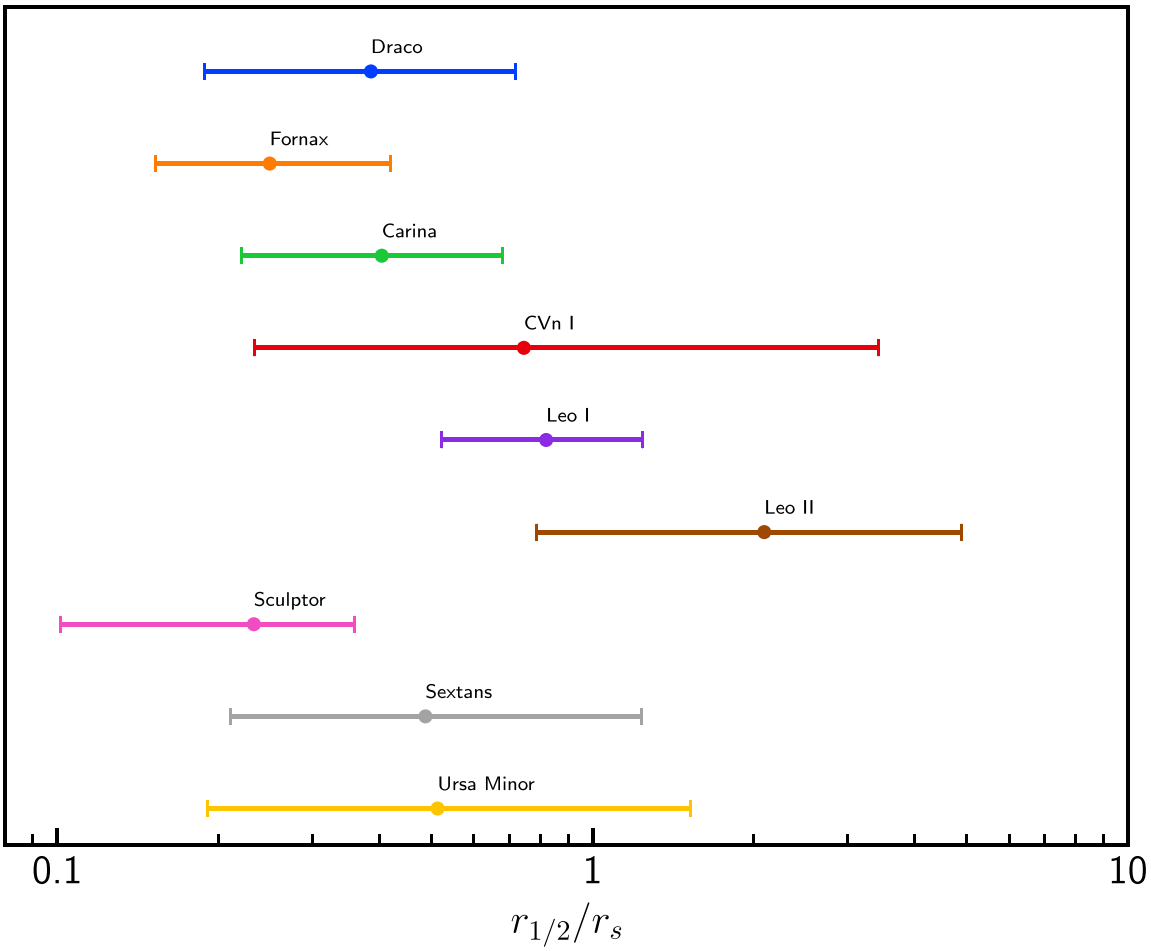

Figure I1. The posterior inference for $r_{1/2}/r_s$, which indicates the degree to which the stellar population is embedded in its DM halo, for the observed sample. The 68 per cent confidence intervals are shown.

APPENDIX J: LINE FIT FOR DENSITY VERSUS PERICENTER

The power-law fit for the density (ρ_{150}) versus pericenter (r_p) data was determined by fitting a line of the form $x = f + gy$, with f and g representing the intercept and slope, respectively. We have defined $x = \log_{10}[r_p/\mathrm{kpc}]$, $y = \log_{10}[\rho_{150}/(10^7 M_\odot \mathrm{kpc}^{-3})]$, with δx and δy corresponding to the uncertainties on x and y, respectively. The fit was determined according to the likelihood

$$\log(\mathcal{L}) = -\frac{1}{2}\sum_i \left(\frac{(x_i - f - g y_i)^2}{\sigma_i^2} + \log\left(2\pi\sigma_i^2\right) \right), \tag{J1}$$

where $\sigma_i^2 = g^2 \delta y_i^2 + \delta x_i^2$. The posteriors are shown in Fig. J1.

Downloaded from https://academic.oup.com/mnras/article/532/4/4157/7718108 by UC - Irvine user on 24 July 2025

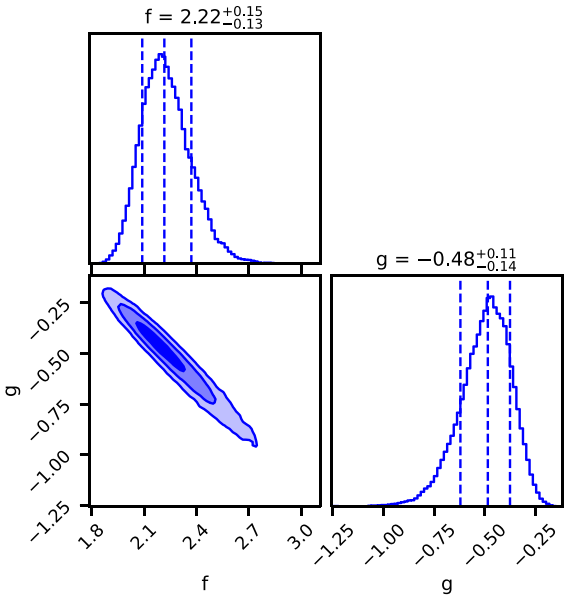

Figure J1. Parameter posteriors and correlation for the best-fitting line of the form $\log_{10}[r_p/\mathrm{kpc}] = f + g \log_{10}[\rho_{150}/(\mathrm{M}_\odot \mathrm{kpc}^{-3})]$. The shaded regions indicate the 1, 2, and 3σ regions, respectively. The dotted lines indicate the 15.9, 50, and 84.1 percentiles, respectively, from left to right.

APPENDIX K: PERICENTER VERSUS DENSITY COMPARISONS FOR ALL PHAT ELVIS HALOES

Here we compare the DM density at 150 pc (ρ_{150}) versus orbital pericenter distance to each of the Phat Elvis haloes (Kelley et al. 2019). We examine subhaloes that are greater than 50 kpc from the galactic center, and show the 20 subhaloes with the largest V_{peak}. Fig. K1 shows the regression for the bright MW dSphs in red, and the host haloes from the Phat Elvis simulation in black and grey.

Downloaded from https://academic.oup.com/mnras/article/532/4/4157/7718108 by UC - Irvine user on 24 July 2025

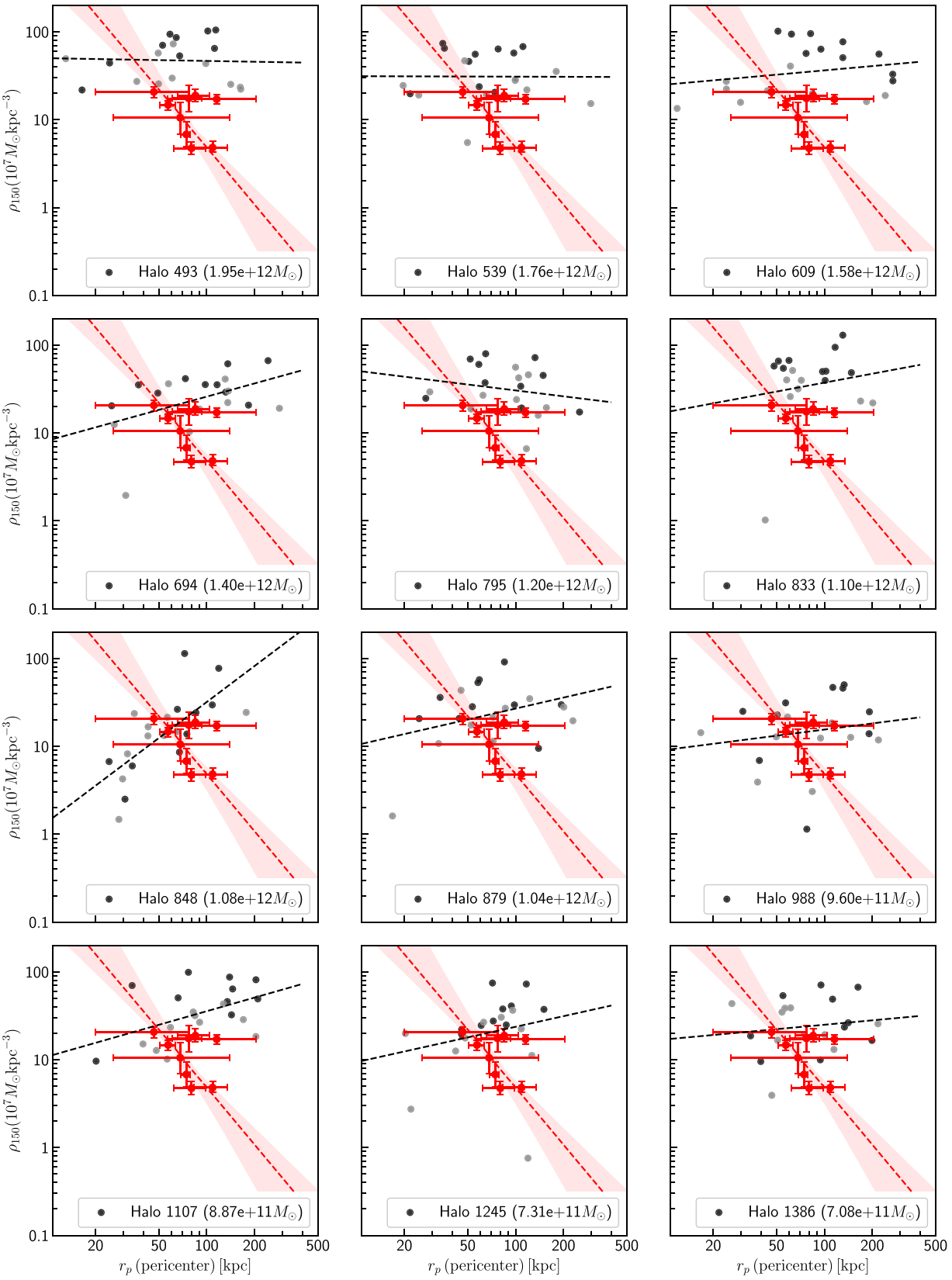

Figure K1. The DM density at 150 pc (ρ_{150}) inferred from the DF fits for the bright MW dSphs versus orbital pericenter distance, in red, compared to the host haloes from the Phat Elvis simulation. For the simulated haloes, the black circles represent the 10 subhaloes with the largest V_{peak} (i.e. the largest V_{max} since their infall) that are currently more than 50 kpc from galactic center. The grey circles denote the 10th through 20th V_{peak} subhaloes.

Downloaded from https://academic.oup.com/mnras/article/532/4/4157/7718108 by UC - Irvine user on 24 July 2025

APPENDIX L: COMPARISON WITH OTHER SOURCES

To address the concern that the heavier MW models of Battaglia et al. (2022) might result in a different result as to the anticorrelation between density and pericenter, we examine the heavier case in Fig. L1. In that figure we use the pericenters from the heavier MW model, with mass $1.6 \times 10^{12} M_{\odot}$. The anticorrelation between ρ_{150} and pericenter is evident. The black and grey dots in the figure are from Phat Elvis halo 609, which has a mass of $1.58 \times 10^{12} M_{\odot}$, the most similar to that of the heavy MW model.

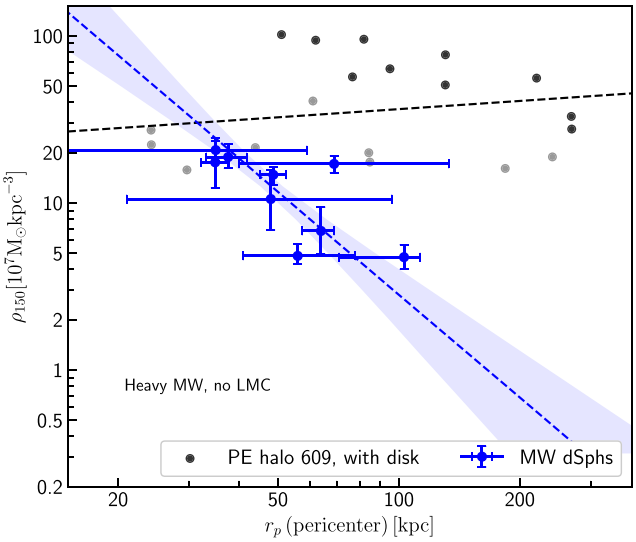

Figure L1. DM density at 150 pc (ρ_{150}) inferred from the DF fits for the bright MW dSphs versus orbital pericenter distance (r_p), in blue, similar to Fig. 14 but now using the heavy MW model of Battaglia et al. (2022) and comparing to host halo 609 of the Phat Elvis simulation (Kelley et al. 2019). The error bars indicate the 68 per cent confidence interval. The best fit line through the observations is shown in dashed blue, with the 68 per cent confidence interval in light blue. The black circles indicate the 10 subhaloes with current radial positions greater than 50 kpc and with the largest V_{peak} for host halo 609 of the Phat Elvis simulation. The grey circles denote the 10th through 20th largest V_{peak} subhaloes. The best-fitting regression line for the Phat Elvis points is shown as a black dashed line.

In Fig. L2, we compare orbital pericenter data from Patel et al. (2020), Battaglia et al. (2022), and Pace et al. (2022). We note the version we adopt in our main analysis in black. The data sets are fairly consistent given their stated uncertainties. The most tension appears in the projections for Sculptor, which has the smallest error bars of the nine dSphs.

In Cardona-Barrero et al. (2023), the authors closely examine the correlation of ρ_{150} with pericenter between a variety of data sets. For central densities, they use the density results of Kaplinghat et al. (2019), Read et al. (2019b), and Hayashi et al. (2020). For pericenter distance they use the data of Fritz et al. (2018), Battaglia et al. (2022), and Pace et al. (2022), some of which have different mass assumptions for the MW and may or may not attempt to account for the LMC. They conclude that the anticorrelation appears statistically significant in some combinations of data sets but not others. Specifically, they find that the Kaplinghat et al. (2019) density data yields a substantial correlation, the Hayashi et al. (2020) data lead to weak correlation, and that the uncertainties in the density are a key determinant of the strength of the correlation. This lends support to our results since the ρ_{150} uncertainties are generally smaller than those of other results. Fig. 13 compares those results, and we point out that we assess an uncertainty which is much smaller than that obtained by Hayashi et al. (2020), which used a completely different method. The caveat here is that spherical symmetry needs to be a good working hypothesis for dSph DM haloes, as our analysis assumes such symmetry but the analysis of Hayashi et al. (2020) does not. Furthermore, Cardona-Barrero et al. (2023) find that the data is better described by models in which the central density ρ_{150} decreases as function of r_p, which contrasts with most of the Phat Elvis simulations (Fig. K1).

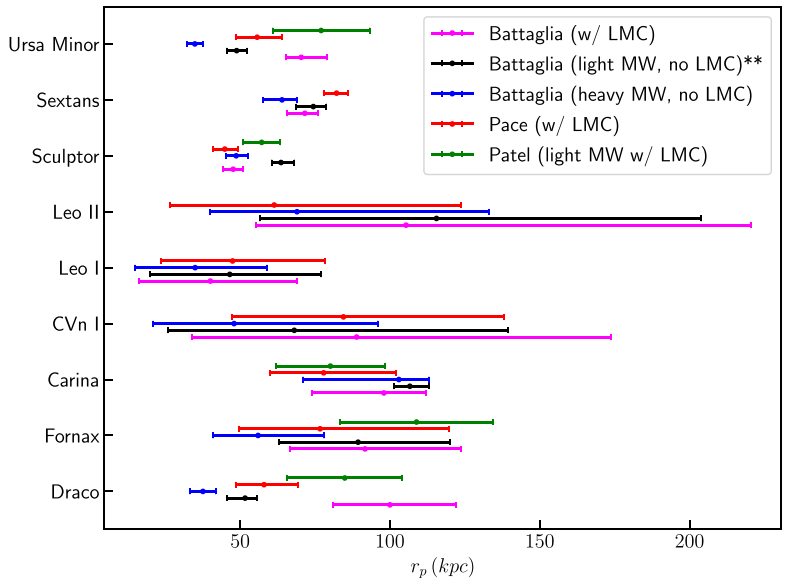

Figure L2. Comparison of recent orbital pericenter data sets. The values used in the main analysis of this work are those of Battaglia et al. (2022)(light MW, no LMC) noted with $**$.

Downloaded from https://academic.oup.com/mnras/article/532/4/4157/7718108 by UC - Irvine user on 24 July 2025

APPENDIX M: PERICENTER REPROJECTIONS FOR PHAT ELVIS SUBHALOES

Here, we examine the impact of using static, axisymmetric potentials and $z = 0$ initial conditions to project subhalo pericenter distances, as is done in Patel et al. (2020), Battaglia et al. (2022), and Fritz et al. (2018). Our subhalo sample is constructed by starting with the subhaloes of all 12 host haloes from the Phat Elvis simulation (Kelley et al. 2019), then selecting the 20 subhaloes with the largest $V_{\rm peak}$ from each host family that are within the host's virial radius. As a starting point for orbital integration, we use the positions and velocities of the subhaloes at $z = 0$, and project backwards in time to find pericenter. The orbital integrations are done in the GALPY software package (Bovy 2015). For each of the 12 host haloes, the potential is based on the 'MWPotential2014' potential of GALPY, which was obtained by fitting to a wide variety of data on the MW. It is the sum of three components: (i) a 'Power Spherical Potential with Cutoff' with mass $4.5 \times 10^9\,{\rm M}_\odot$, (ii) a Miyamoto Nagai Potential with mass $6.81 \times 10^{10} M_\odot$, and (iii) an NFW potential. For our purposes, the NFW component's mass is adjusted so that the sum of the masses of the modelled potentials are the same as that of the corresponding Phat Elvis host halo.

Fig. M1 compares the reprojections of pericenter using the method described above to the true values for the Phat Elvis subhaloes. In general, there is good agreement with the true value, although the reprojections exhibit a mild tendency to be underestimated, and there are more outliers on the side of underprojection. The 16th, 50th, and 84th percentile values of the errors are −0.14, −0.01, and 0.05 dex, respectively, as shown in the histogram of Fig. M2.

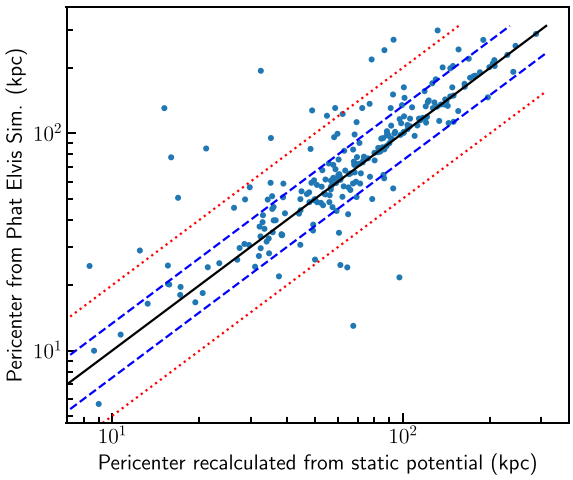

Figure M1. Comparison of the true pericenter distances (y-axis) with projections of pericenter using a static, axisymmetric potential (x-axis) for the subhaloes with the largest $V_{\rm peak}$ in the 12 Phat Elvis hosts. The solid black line indicates equality, the dashed blue line indicates 25 per cent error, and the dotted red line indicates 50 per cent error.

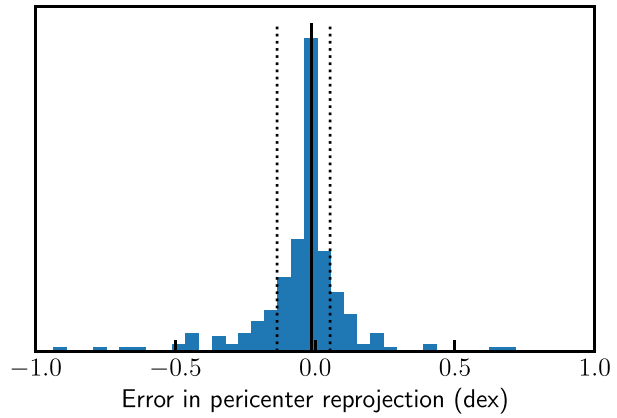

Figure M2. A histogram of the error between the reprojected pericenters and the true values from the Phat Elvis simulation, in dex (i.e. $\log_{10}[{\rm peri}_{\rm reproj}/{\rm peri}_{\rm true}]$). The 16th, 50th, and 84th percentile values are indicated with vertical lines.

APPENDIX N: POSSIBLE EFFECTS FROM TIDAL TRUNCATION

As a satellite galaxy falls into the potential well of our Galaxy, the outer part of the satellite's DM halo may become stripped by tidal forces, resulting in a DM profile that may not be well modelled by the cNFW profile. To investigate the possible effects of this tidal truncation, we calculate the radius of truncation based on the method in Jiang et al. (2021), equation (S9), which is

$$r_{\rm t}^3 \approx r^3 \left(m_{\rm sat}(r_{\rm t})/M_{\rm host}(r)\right) \Big/ \left(2 - {\rm d}\ln M_{\rm host}/{\rm d}\ln r + v_{\rm tan}^2/v_{\rm circ}^2\right)\,, \tag{N1}$$

where $r_{\rm t}$ is the tidal truncation radius of the satellite, $m_{\rm sat}(r_{\rm t})$ is the mass of the satellite within the tidal truncation radius, r is the distance of the satellite from the host centre, $M_{\rm host}(r)$ is the mass of the host galaxy within radius r, $v_{\rm tan}$ is the tangential velocity of the satellite, and $v_{\rm circ}$ is the circular velocity of the host potential at the radius in question. For $m_{\rm sat}(r_{\rm t})$, we compute the mass using the cNFW profile. For $M_{\rm host}(r)$, we use the 'MWPotential2014' model in the GALPY software package (Bovy 2015).

For our purposes, we wish to calculate the truncation radius at pericenter, as any satellite that has made at least one pericenter passage will have been truncated to the maximum extent. To obtain the tangential velocity at pericenter, we assume that the satellite's motion conserves angular momentum about the galactic center, so that $v_{\rm tan}(r_{\rm p}) = v_{\rm tan}(r_0) r_0/r_{\rm p}$. For consistency, we use Fritz et al. (2018) Tables 2 and 3 for the values of $v_{\rm tan}(r_0)$, r_0 and $r_{\rm p}$, corresponding to their Milky Way mass model with mass $10^{12}\,{\rm M}_\odot$. The resulting truncation radii $r_{\rm t}$ and the ratios for $r_{\rm t}/r_{\rm max}$ for the observed sample are shown in Table N1. None of the satellites in the sample are severely truncated. Relative to their $r_{\rm max}$, the most truncation occurs in Sextans and Ursa Minor.

Downloaded from https://academic.oup.com/mnras/article/532/4/4157/7718108 by UC - Irvine user on 24 July 2025

Table N1. Calculated tidal radii for the bright MW dSphs, as compared to r_{max} and in kpc. The median posterior value and the 68 per cent confidence intervals are indicated.

MW dSph Name	r_t/r_{max}	r_t(kpc)
Draco	$1.40^{+0.89}_{-0.56}$	$3.61^{+2.28}_{-1.36}$
Fornax	$1.48^{+0.66}_{-0.63}$	$20.00^{+10.20}_{-8.59}$
Carina	$1.60^{+0.36}_{-0.47}$	$10.69^{+3.60}_{-3.21}$
CVn I	$2.22^{+3.80}_{-1.65}$	$5.04^{+6.63}_{-3.89}$
Leo I	$3.14^{+5.19}_{-2.20}$	$4.44^{+7.54}_{-3.10}$
Leo II	$4.79^{+10.75}_{-3.47}$	$3.62^{+7.81}_{-2.62}$
Sculptor	$1.66^{+0.53}_{-0.51}$	$7.09^{+3.00}_{-1.76}$
Sextans	$1.29^{+0.77}_{-0.42}$	$4.67^{+1.77}_{-1.20}$
Ursa Minor	$1.34^{+1.20}_{-0.59}$	$3.73^{+2.66}_{-1.46}$

As a check on the possible impact of tidal truncation on our models, we modelled an abruptly truncated halo with truncation radius of 1.5 r_{max}. That is, we define a new profile as follows:

$$\rho(r) = \begin{cases} \rho_{NFW}(r), & r <= 1.5 r_{max}, \\ 0, & r > 1.5 r_{max} \end{cases} \quad \text{(N2)}$$

We chose $1.5 r_{max}$ as a test value because several of the observed dSphs in Table N1 have truncation radii approximating that value. We reran the DF model using this density profile and its associated potential for three of the observed dSphs: Draco, Sextans and Ursa Minor. We found that the impact of the truncation is modest, with r_{max} increasing 0.1 to 0.2 dex, V_{max} increasing typically ≈ 0.1 dex, and ρ_{150} decreasing 0 to 0.2 dex. A more robust approach would be to allow the truncation radius to be a varying parameter in the model; we hope to do so in future work. At present, we are satisfied that abrupt tidal truncation at $1.5 r_{max}$ does not seem to have a strong impact on our inferences.

APPENDIX O: MOCK DATA CHARACTERISTICS

In the Table O1, we report the main ingredients characterizing the mock data set analysed in our study.

Downloaded from https://academic.oup.com/mnras/article/532/4/4157/7718108 by UC - Irvine user on 24 July 2025

Table O1. Mock data characteristics. The columns, from left, are (1) ID number, (2) ID string, (3) the number of stars in the data set, (4) DM profile type, (5) log slope of the inner stellar profile, (4) scale radius of the stellar profile, (6) anisotropy radius of the stellar profile, (7) 3D half-light radius, and (8) VSP of the data set.

Number	ID	w	DM profile	γ_*	r_* (kpc)	r_a (kpc)	$r_{1/2}$ (kpc)	VSP (10^3 km^4/sec^4)
1	aaaO-4639	4639	Cored	0.1	0.1	1	0.122	$4.25^{+1.59}_{-0.75}$
2	aabO-4941	4941	Cored	0.1	0.1	10000	0.119	$3.08^{+0.62}_{-0.43}$
3	abaO-1801	1801	Cored	0.1	0.25	1	0.310	$25.87^{+6.29}_{-3.95}$
4	abbO-5483	5483	Cored	0.1	0.25	10000	0.300	$23.00^{+2.20}_{-1.79}$
5	acaO-3904	3904	Cored	0.1	0.5	1	0.596	$94.09^{+10.67}_{-7.99}$
6	acbO-2607	2607	Cored	0.1	0.5	10000	0.588	$84.75^{+12.34}_{-9.30}$
7	adaO-1980	1980	Cored	0.1	1.0	1	1.233	$231.66^{+25.55}_{-22.09}$
8	adbO-1441	1441	Cored	0.1	1.0	10000	1.251	$172.54^{+15.29}_{-14.22}$
9	baaO-1826	1826	Cored	1.0	0.1	1	0.093	$2.89^{+2.26}_{-0.80}$
10	babO-2156	2156	Cored	1.0	0.1	10000	0.090	$1.80^{+0.72}_{-0.40}$
11	bbaO-1776	1776	Cored	1.0	0.25	1	0.238	$17.31^{+5.25}_{-3.04}$
12	bbbO-3368	3368	Cored	1.0	0.25	10000	0.227	$15.07^{+2.67}_{-1.87}$
13	bcaO-2107	2107	Cored	1.0	0.5	1	0.463	$70.06^{+12.83}_{-9.49}$
14	bcbO-2349	2349	Cored	1.0	0.5	10000	0.464	$50.70^{+8.25}_{-5.63}$
15	bdaO-2677	2677	Cored	1.0	1.0	1	0.913	$164.09^{+17.59}_{-14.81}$
16	bdbO-2456	2456	Cored	1.0	1.0	10000	0.914	$113.42^{+8.75}_{-8.47}$
17	aaaN-2358	2358	NFW	0.1	0.1	1	0.121	$3.73^{+0.45}_{-0.39}$
18	aabN-3539	3539	NFW	0.1	0.1	10000	0.122	$3.04^{+0.23}_{-0.21}$
19	abaN-2975	2975	NFW	0.1	0.25	1	0.294	$12.40^{+1.23}_{-1.04}$
20	abbN-4239	4239	NFW	0.1	0.25	10000	0.300	$9.06^{+0.52}_{-0.47}$
21	acaN-1088	1088	NFW	0.1	0.5	1	0.600	$20.78^{+2.64}_{-2.22}$
22	acbN-550	550	NFW	0.1	0.5	10000	0.603	$15.12^{+2.46}_{-2.17}$
23	adaN-1860	1860	NFW	0.1	1.0	1	1.238	$30.86^{+3.40}_{-2.96}$
24	adbN-826	826	NFW	0.1	1.0	10000	1.226	$23.92^{+3.38}_{-2.76}$
25	baaN-1533	1533	NFW	1.0	0.1	1	0.096	$2.96^{+0.49}_{-0.36}$
26	babN-1491	1491	NFW	1.0	0.1	10000	0.092	$2.43^{+0.37}_{-0.28}$
27	bbaN-1214	1214	NFW	1.0	0.25	1	0.238	$6.68^{+0.75}_{-0.65}$
28	bbbN-1153	1153	NFW	1.0	0.25	10000	0.224	$7.27^{+0.76}_{-0.71}$
29	bcaN-2054	2054	NFW	1.0	0.5	1	0.453	$16.46^{+1.61}_{-1.40}$
30	bcbN-1222	1222	NFW	1.0	0.5	10000	0.434	$14.89^{+1.57}_{-1.38}$
31	bdaN-2912	2912	NFW	1.0	1.0	1	0.953	$25.33^{+2.03}_{-1.80}$
32	bdbN-1524	1524	NFW	1.0	1.0	10000	0.925	$24.24^{+2.18}_{-2.07}$

This paper has been typeset from a TEX/LATEX file prepared by the author.

Downloaded from https://academic.oup.com/mnras/article/532/4/4157/7718108 by UC - Irvine user on 24 July 2025

© 2024 The Author(s).
Published by Oxford University Press on behalf of Royal Astronomical Society. This is an Open Access article distributed under the terms of the Creative Commons Attribution License (https://creativecommons.org/licenses/by/4.0/), which permits unrestricted reuse, distribution, and reproduction in any medium, provided the original work is properly cited.